COLOR FIELDS AROUND THE STATIC QUARK–ANTIQUARK PAIR*

T. BARCZYK

Particles Theory Department, Institute of Physics
Jagellonian University

(Received March 8, 1995)

We carried out an extensive study of the distribution of the color fields around the static $q\bar{q}$ pair using the methods of lattice field theory. The measurements have been performed on Monte Carlo configurations with dynamical fermions, at $\beta = 5.35$, on the $16^3 \times 24$ lattice with periodic boundary conditions. We have found some interesting differences with the quenched results published earlier, among them the effect of breaking the flux tube. We also performed perturbative calculations up to one loop level to see which details of the color field distribution obtained using MC methods are purely nonperturbative and which can be understood from the perturbative expansion of the QCD action.

PACS numbers: 12.38.Gc

1. Introduction

1.1. Confinement of quarks

In the last 30 years many experimental and theoretical arguments appeared supporting the idea of quarks and gluons as elementary strongly interacting particles of the nature. This evidence comes from isospin and SU(3) flavor symmetries, the results of the deep inelastic lepton–hadron scattering and the spectroscopy of the low energy excited states of hadrons and the ψ and Υ particles. Nevertheless, neither the free quarks nor gluons have been ever observed. This led to the idea of confinement — the long distance attractive interquark force which prohibits quarks separation thus allowing only for the existence of their bound states — hadrons. Until now there is still no rigorous theoretical proof of this phenomenon although many models have been created to explain it.

* Work supported by Polish Government under KBN grant 2P30204705.

In the model presented by Kogut and Susskind [1] the confining force is connected with the formation of the electric flux tube between charges, with finite energy per unit length. Similar effect can be observed in the superconductors of the second kind. As a result of applying strong external magnetic field the magnetic flux tube is created in such materials in the form of fibres of non-superconductive medium.

Another model of confinement, which was widely explored, has been suggested by Chodos *et al.* [2] . According to them the hadron is made of quarks and gluons confined inside a finite region (a bag) with a constant energy per unit volume. It was achieved by imposing appropriate boundary conditions which do not allow the particles to be separately extracted outside the bag. Despite of its conceptual simplicity, this model (MIT bag model) was able to explain many observed features of hadrons.

The most widely accepted candidate for the theory of strong interactions is the Quantum Chromodynamics (QCD) based on the color SU(3) gauge group. One expects to obtain the effect of confinement in this theory as a consequence of its complicated nonabelian structure connected with new color degrees of freedom [3]. It leads in turn to the nonzero coupling between gluons which makes the interaction qualitatively different comparing, for instance, to the case of Quantum Electrodynamics. In QCD, nonperturbative treatment is needed when investigating the long–range part of quark interactions responsible for confinement. It forces the use of special techniques, among them Lattice Field Theory and Monte Carlo simulations [4–7].

1.2. Lattice field theory — a nonperturbative method of exploring QCD

Lattice QCD is a discretized Yang–Mills theory with dynamical quarks. It was first formulated by Wilson [5]. The motivation was to provide a systematic, nonperturbative method of handling field theory with coupling constant becoming large at large distances. This behavior, characteristic for QCD, is qualitatively different than in QED and makes it impossible to treat this theory in standard, perturbative way.

Lattice QCD is a regularized theory. On a lattice, wavelengths less than the double lattice spacing a are meaningless. This implies that the momenta are automatically cut off thus removing the ultraviolet infinities. Physical results can be recovered in the continuum limit of this theory ($a \to 0$), after applying the renormalization procedure. The formulation of the QCD on a lattice also preserves exact local gauge invariance.

There is also an important practical feature of this theory. Since it is formulated on a discrete lattice, it is well suited for numerical calculations. After quantization using Feynman path integrals and continuation to the euclidean time, it closely resembles statistical physics with the partition

function equal to Feynman quantum amplitude. This in turn allows for using standard statistical methods (high and low temperature expansions, Monte Carlo simulations).

Lattice field theory has a computable strong coupling limit in which the confinement arises. Historically, it was the first major success of this theory and the whole subsequent work was devoted to showing that this property persists for finite coupling as well.

The degrees of freedom of the lattice Yang–Mills theory are link variables U_l being members of the considered gauge group. In the case of SU(3) they are unitary 3×3 matrices associated with gauge fields A_l

$$U_l = \exp\left(\mathrm{i}g_0 a A_l\right) = \exp\left(\mathrm{i}g_0 a A_l^a T^a\right) , \tag{1}$$

where g_0 is the bare coupling constant, a is the lattice spacing and the index l represents oriented link between neighbouring sites $x, x+\hat{\mu}$ (such link can also be denoted (x,μ)). The T^as are the group generators.

The gauge invariant Wilson action is defined as follows

$$S^{\mathrm{W}} = \sum_{\square} \beta\left(1 - \mathrm{Re}P_{\square}\right) , \tag{2}$$

where $\beta = 2n/g_0^2$, n is the dimension of the fundamental representation of the gauge group and $P_{\square}$ denotes plaquette — an elementary gauge invariant object constructed from four links forming a closed loop

$$P_{\square}(x) = \frac{1}{n}\mathrm{Tr}U_{x,\mu}U_{x+\mu,\nu}U^{\dagger}_{x+\nu,\mu}U^{\dagger}_{x,\nu} . \tag{3}$$

We used the definition $U_{x,-\mu} \equiv U^{\dagger}_{x-\mu,\mu}$.

The plaquette is an example of a more general gauge invariant object on a lattice — the Wilson loop

$$W = \frac{1}{n}\mathrm{Tr}\prod_{l\in W} U_l , \tag{4}$$

where, for simplicity, the symbol W denotes also the actual loop formed by the links l.

Fermions are introduced by adding appropriate gauge invariant term to the action

$$S^{\mathrm{F}} = \tfrac{1}{2}\mathrm{i}a^3 \sum_{x\mu}\left(\overline{\psi}_x\gamma_\mu U_\mu(x)\psi_{x+\mu} - \overline{\psi}_{x+\mu}\gamma_\mu U^{\dagger}_\mu(x)\psi_x\right) - m_0 a^4 \sum_x \overline{\psi}_x\psi_x . \tag{5}$$

Here m_0 is the bare mass and $\psi_x, \overline{\psi}_x$ — the fermionic fields located at the point x. This action has a correct classical continuum limit, but leads to

the problem of *species doubling* [7]. This usually requires the reformulation of the fermionic part of the theory by introducing additional terms to the action (*Wilson fermions*) or decomposing the lattice into an even and odd sublattices (*staggered* or *Kogut–Susskind fermions*).

Now we introduce some basic definitions used throughout this work. The quantum expectation value of a lattice observable X is defined as

$$\langle X \rangle = \frac{1}{Z} \int [\mathrm{d}U] X \mathrm{e}^{-S[U]}, \tag{6}$$

where $[\mathrm{d}U]$ is the measure, Z — the normalization factor (partition function)

$$Z = \int [\mathrm{d}U] \mathrm{e}^{-S[U]} \tag{7}$$

and $S[U]$ — the total action of the theory.

The correlation function of two observables X and Y can be written as

$$\langle XY \rangle = \frac{1}{Z} \int [\mathrm{d}U] XY \mathrm{e}^{-S[U]}. \tag{8}$$

These formulas can be evaluated analytically (Section 4) or numerically, using Monte Carlo simulations (Section 2).

1.3. Survey of studies of the fields around two static quarks

The research on the structure of the color fields around the static charges is a next advance towards the understanding of the physics of strong interactions and the origin of confinement. It allows not only to obtain the dependence of the $q\bar{q}$ potential on the distance but also enables the more detailed exploration of the local behavior of particular components of the chromoelectric and chromomagnetic fields. Using methods developed recently, in connection with the significant progress in computer technology in the last ten years, one can now determine the shape of the flux tube between the $q\bar{q}$ pair with respect both to the energy and action densities and its dependence on the interquark distance. Other issues that can be investigated in this field include asymptotic freedom (Coulomb limit) and excited states of the string.

First, exploratory study of the problem of the energy density distribution around static $q\bar{q}$ pair using Monte Carlo techniques was carried out for SU(2) by Fukugita and Niuya in 1983 [8]. They pointed out the general domination of the electric flux components (over the magnetic ones) and noticed, that the transverse thickness of the flux tube increases with the interquark distance in qualitative agreement with the string model. Also,

the resemblance of the system to the electric dipole was observed. Analogous work was done for the SU(3) case in 1985 by Flower and Otto [9] with the stress on the connections with the string model. Large scale Monte Carlo simulations were performed during 1987-1989 by the Cracow — LSU collaboration [10–13], revealing the shape of the flux tube for large quark separations (up to 9 lattice units). Lattice action and energy sum rules obtained by Michael [9] were thoroughly checked in this work. Extensive studies of the color flux distribution in the presence of static quarks were also done by Sommer [15, 16]. Althouhg different operators were used the results are consistent with the other ones. Field distribution around adjoint source was considered by Jorysz and Michael [17]. Another important contribution to the understanding of these issues is the recent work of Bali and Schilling [18]. They used quite large lattices (up to $48^3 \times 64$) to demonstrate flux tube formation over large physical distances in quenched SU(2) gauge theory.

All these results were produced in the so called quenched approximation which means that the loops of virtual light quarks were neglected [19–21]. Also, most of authors dealt with SU(2). In the last years new opportunities of studying the structure of the flux tube arose. Thanks to continuous development of both computer technology and numerical algorithms we are now in a position to include the effects of dynamical fermions in our measurements. First such study was carried out by Feilmar and Markum [22] for SU(3). They measured Polyakov loops on $8^3 \times 4$ lattice restoring most important results of the quenched approximation. They also claimed to find the evidence of the breaking of the flux tube although small N_t size does not allow to rule out the finite temperature effects in this case. The breaking of the tube is a qualitatively new effect introduced by dynamical fermions.

In this dissertation we present the results for SU(3) and much bigger ($16^3 \times 24$) lattice based on MT_c configurations with dynamical fermions [23–25].

1.4. Purpose of this work

The main aim of this work is the presentation and analysis of the results of the measurements of the distribution of the color fields around the static $q\bar{q}$ pair. The novelty of these measurements is that they were performed on SU(3) configurations with dynamical fermions, *i.e.* without the quenched approximation.

Apart from these measurements we also carried out extensive analytic calculations of the same quantities for SU(3) in weak coupling approximation up to one loop level. The formulas obtained analytically were worked out in configuration space using efficient numerical methods (Fast Fourier

Transform). Comparing the numerical Monte Carlo results with the perturbative ones can help in filtering out perturbative effects in an attempt to understand purely nonperturbative phenomena. The MC results obtained in this work have also been compared with analogous measurements published earlier by many people and computed using quenched approximation (*cf.* Section 1.3). The effect of the introduction of dynamical fermions is especially interesting. Also, the quality of the quenched approximation, used until now, can be assessed.

In Section 2 we introduce the Monte Carlo method in lattice field theory and show how this method can be used to reveal the details of the distribution of the color fields around static quarks. In Section 3 we present the results of the measurements based on MC simulations with dynamical fermions. Although, in general, our results coincide with the quenched ones, we observe an important difference in the field distribution connected with the introduction of dynamical fermions. Energy and action sum rules are also analysed in this section leading to additional interesting conclusions. Finally, we present an alternative promising method of computing the flux distribution. In Section 4 we show how the color fields distribution analysed in previous sections can be calculated analytically using perturbative expansion on the lattice. We derive appropriate formulas in the tree and one loop order. In Section 5 the results of numerical evaluation of the formulas derived in section 4 are presented. We contrast them with the Monte Carlo results which proves the nonperturbative origin of the flux tube.

2. Color fields around the $q\bar{q}$ pair from Monte Carlo simulations with dynamical fermions

2.1. Monte Carlo methods in lattice gauge theory

Monte Carlo methods are widely used in statistical physics. They are an important tool in all cases where analytic results cannot be obtained. Since the lattice formulation of the Quantum Chromodynamics in Euclidean space (Section 1.2) is equivalent to the statistical physics with the partition function Z given by (7) these methods can be directly applied in this field [4, 27, 28].

The usual method of working out Eq. (6) using the Monte Carlo simulation involves generation of some (large) number of configurations $\{U\}$ (sets of link variables U) with probability governed by the Boltzmann distribution $P(U) \sim \mathrm{e}^{-S[U]}$ (β was absorbed into S for simplicity) [1]. Then

[1] We write U instead of $\{U\}$ to simplify the notation

the equilibrium expectation value of some quantity X can be directly obtained as an ordinary average of the values which it takes for particular configurations

$$\langle X \rangle = \frac{1}{N} \sum_{n=1}^{N} X[U_n], \tag{9}$$

with the error decreasing as $1/\sqrt{N}$ provided the subsequent configurations are not correlated.

In practice, a Markov chain of succesive configurations C is generated, in which a configuration C_n depends only on the previous one, C_{n-1}, and the so called *detailed balance condition* is satisfied. In the case of Boltzman distribution this condition has the form:

$$P(C_n \to C_{n+1}) \exp(-S[C_n]) = P(C_{n+1} \to C_n) \exp(-S[C_{n+1}]). \tag{10}$$

This condition ensures that if the configuration C_n obtained after some steps is distributed according to Boltzman distribution, the next one, C_{n+1} also has the same probability distribution. If, in addition, the process is *ergodic* which means that any configuration in the chain can be reached starting from any other one (the configuration space does not split into disconnected parts) the sequence of C_ns converges to the required probability distribution[2].

Two algorithms of generating configurations with given probability are widely known and form the basis for more sophisticated ones — the *heat bath* method and the *Metropolis* method [4, 7, 29]. In the elementary step of the heat bath algorithm every link variable U_l is choosen according to the required distribution as if it were in thermal contact with a background of all links interacting with it. In the Metropolis algorithm a modification of the link variable is proposed and accepted or rejected with a probability determined by the change in the total action generated by this modification.

2.2. Monte Carlo for dynamical fermions

Simple algorithms mentioned in the previous section become very time consuming in cases when the change of action between succesive configurations is nonlocal *i.e.* requires recomputing of the whole action instead of being obtained as a function of a few locally modified variables [4]. An example of such a situation is the lattice MC simulation of the QCD with dynamical fermions. In this case the partition function Z has the general form

---

[2] The process of approaching the equlibrium distribution is called *thermalization*

$$Z = \int [\mathrm{d}U \mathrm{d}\psi \mathrm{d}\overline{\psi}] \mathrm{e}^{-S[U] - S_{\mathrm{F}}[U,\psi,\overline{\psi}]}, \tag{11}$$

with ψ and $\overline{\psi}$ being the fermionic fields and S_{F} — the fermionic part of the action. Integration over Grassman variables

$$\int [\mathrm{d}\psi \mathrm{d}\overline{\psi}] \mathrm{e}^{-\overline{\psi} M \psi} = \det M, \tag{12}$$

leads to the following formula which, in principle, can be directly used in the MC simulation

$$Z = \int [\mathrm{d}U] \det M[U] \mathrm{e}^{-S[U]} = \int [\mathrm{d}U] \mathrm{e}^{-S_{\mathrm{eff}}}. \tag{13}$$

Here M is the fermionic matrix defined by $S_{\mathrm{F}} = \overline{\psi} M \psi$, which is very large, extremely sparse (at least for typical fermion actions) and, unfortunately, $\det M$ depends nontrivially on the whole configuration of the Us. This makes the S_{eff} used in simulation nonlocal. The simplest approximation possible at this point is to neglect the fermionic determinant altogether and generate configurations according to pure gauge measure [19–21]. It implies leaving out all effects from internal quark loops and, consequently, fermions are not dynamical in this approximation. This theory (quenched approximation) was simulated in the 80s and up to now as the only one technically accessible.

In practice, direct MC simulation of the full QCD using (13) is never performed. Replacing the determinant by an integral over a set of auxiliary bosonic fields χ^* and χ leads to

$$Z = \int [\mathrm{d}U \mathrm{d}\chi^* \mathrm{d}\chi] \mathrm{e}^{-S[U] - \chi^* M^{-1} \chi}. \tag{14}$$

Now updating every link variable requires only the recalculation of the $\chi^* M^{-1} \chi$ which is much simpler than inversing the whole matrix. Many effective algorithms of solving the corresponding linear (Dirac) equation

$$M \boldsymbol{x} = \chi \tag{15}$$

have been developed, among them methods based on Conjugate Gradients algorithms [30–32], Incomplete LU Decomposition [30, 32], Multigrid [32–34] and Alternate Direction Implicit method [35]. Since the recalculation after each link update is still very time consuming many approximate variants of this method have been devised. Most of them are based on solving (15) once after all Us have been updated.

There are, however, exact methods which also require this inversion to be performed only once per lattice sweep. They use global configuration updates instead of local ones and Metropolis type accept/reject step to control detailed balance condition [36, 37]. The Hybrid Monte Carlo Algorithm (HMCA) [36] is the one which combines the features of the Molecular Dynamics method [38] and Langevin type step [39]. In this algorithm the global updates are performed as a result of the microcanonical evolution of the whole configuration with artificially introduced momenta and time. This ensures higher acceptance ratios which was generally a problem in global update schemes. The simulated probability is now

$$e^{-\frac{1}{2}p^2 - S[U] - \chi^* M^{-1} \chi}, \tag{16}$$

with the ps as conjugated momenta allowing to construct the "phase space" and the "Hamiltonian". An elementary step $t \to t'$ of the HMCA consists of generating the momenta according to Gaussian distribution, then evolving p and U for the time t' using equations of motion and the Leapfrog method, and finally accepting or rejecting the new configuration according to Metropolis criterion. The χ field is updated in between using $\chi = M\xi$ with Gaussian noise ξ .

The configurations analyzed in this work to measure the $\langle WP \rangle$ correlations were produced by the MT_c collaboration using the HMCA algorithm [23].

2.3. Field distribution from Monte Carlo data — the method

The components of the chromoelectric and chromomagnetic field around the static $q\bar{q}$ pair can be expressed in terms of correlations between the Wilson loop oriented in the space-time plane (with the spatial extent R equal to the interquark distance) and appropriately chosen plaquettes

$$f_{\mu\nu}(x) = \frac{\beta}{a^4} \frac{\langle W P_{\mu\nu}(x) \rangle - \langle W \rangle \langle P_{\mu\nu}(x) \rangle}{\langle W \rangle}, \tag{17}$$

where W denotes the Wilson loop and $P_{\mu\nu}(x)$ the plaquette oriented in the plane $\mu\nu$ with the center at x [8–10].

In the classical continuum limit ($a \to 0$) the average value of the square of particular components of the color field at the space-time point x is reproduced

$$f_{\mu\nu} \to -(\tfrac{1}{2}) \langle F_{\mu\nu}^2 \rangle, \tag{18}$$

so that $-2f_{ik}$ represent squared magnetic components of the color fields and $2f_{i4}$ squared electric ones in the Minkowski space. Therefore, in order

to find the distribution of the field around the static $q\bar{q}$ pair, one needs to measure the expectation value of the Wilson loop and the correlations between the loop and plaquettes.

In (18) and throughout this work we use the simplified notation

$$\langle F_{\mu\nu}^2 \rangle \equiv \langle F_{\mu\nu}^2 \rangle_{q\bar{q}} - \langle F_{\mu\nu}^2 \rangle_{\text{vacuum}}, \tag{19}$$

where $\langle\rangle_{\text{vacuum}}$ means the quantum average in the vacuum state and $\langle\rangle_{q\bar{q}}$ — the average in the $q\bar{q}$ sector of the Hilbert space.

The formula (17) can be approximated as

$$f_{\mu\nu}(x) = \frac{\beta}{a^4} \frac{\langle WP_{\mu\nu}(x) - WP_{\mu\nu}(\infty) \rangle}{\langle W \rangle}, \tag{20}$$

where $P_{\mu\nu}(\infty)$ denotes "plaquette at infinity" in practice chosen as lying at the maximal distance from the Wilson loop (on the periodic lattice), where we believe the correlations vanish (actually they vanish much closer to the Wilson loop [11]). Eq. (20) has an advantage of giving much smaller errors due to self-cancellations of the statistical fluctuations of the terms inside the brackets [10].

2.4. Details of the measurements

The measurements have been performed on 80 MT_c configurations with dynamical fermions [23], at $\beta = 5.35$ ($a = 0.125$ fm), on the $16^3 \times 24$ lattice with periodic boundary conditions [24, 25]. Apart from the simple error reducing trick mentioned in Section 2.3, the smearing technique has been used to improve the signal by decreasing the fluctuations of the link variables. Every space-like link has been replaced by the normalized combination of 4 oriented products of links, *staples*, surrounding it

$$U_\mu(n) \sim U_\nu(n) U_\mu(n+\nu) U_\nu^\dagger(n+\mu) + \text{three other staples}, \tag{21}$$

where $\mu, \nu \neq 4$.

The measurements of the $\langle W \rangle$ and the $\langle WP \rangle$ correlations for particular Monte Carlo configuration have been performed making use of the following lattice symmetries:

1. Translational symmetry — the Wilson loop and the plaquette can be simultaneuously shifted along any of the four space-time axes, which produces $16^3 \times 24$ quasi independent values.
2. Rotational symmetry — the Wilson loop can be located in three planes xt, yt, zt which multiplies the number of sampled values obtained from

one configuration by 3 (other possible Wilson loop orientations could not be used due to the space-time asymmetry of the lattice).

3. Reflection symmetry — there are 16 equivalent plaquette locations around the Wilson loop (symmetric *quadrants*) which yield an additional factor of 16 measurements per configuration.

Therefore, the final value of the correlation between the Wilson loop and the plaquette, obtained from one configuration, is the average of $16^3 \times 24 \times 3 \times 16 = 4,718,592$ measurements. The averaging over translationally symmetric measurements have been done using the *discrete correlation theorem* and the Fourier Transform (the details are given in Appendix A). This method produces at once all averaged results for various relative orientations of the Wilson loop and the plaquette and can dramatically accelerate computations when applying the Fast Fourier Transform (FFT) algorithm (which can be further effectively vectorized for the vector computer).

The MC configurations have been grouped into 16 bins, each of 5 consecutive configurations, to decorrelate the data. Each bin was the input for one program run, which produced the averaged results for all Wilson loops in the range 1×1 to 8×8. The final statistical error was estimated as the standard deviation of the population of these bins.

The reference plaquette, *cf.* Eq. (20), was chosen to be placed at the maximal possible distance from the Wilson loop, contrary to the *fiducial volume* approach used in [11]. However, the subspace for which the results have been saved on disk and then used for statistical analysis was limited to the 4-dimensional cuboid with the sides extending 4 lattice units in each direction from the Wilson loop.

The FORTRAN program for computing the correlations was prepared in Kraków during 1991. Final tests and code vectorization was carried out at the computer center of the KFA Jülich, Germany. Main computations and statistical analysis of the results were performed in 1991–1992 on the Cray Y-MP supercomputer at this center, partially from Kraków using Internet capabilities. All required interpolations and data smoothing was done on IBM RISC workstation at Particles Theory Department, Institute of Physics, Jagellonian University in 1992–1993.

3. Monte Carlo results

We begin with describing the notation and geometry which will be used throughout this section. Independently of whether we present the Monte Carlo or the analytic results, the general set-up of the lattice is the same:

1. The 4-dimensional lattice is assumed to be periodic in all dimensions. Its size is $N_V = N_1 \times N_2 \times N_3 \times N_4$ sites so that it consists of $4N_V$

links. Most often we will consider the case of symmetric lattice $N_1 = \ldots = N_4 \equiv N$.

2. The Wilson loop of the size $R \times T$ lies in the zt plane. The interquark line is the z axis (the longitudinal direction). The mid–point between the quarks is $(0,0,0,0)$ (for the timeslice $T = 0$) and the corners of the loop are $(0,0,\pm R/2,\pm T/2)$. The directions x and y are collectively called the transverse directions. We denote the longitudinal direction by Z and the transverse direction by X in all figures. We use lattice units for the space-time coordinates.
3. There are six possible orientations of the plaquettes according to the six components of the color field tensor. Since we have chosen the Wilson loop to be oriented in zt plane, the relationship between various plaquettes and the field components is as follows:

component	plaquette
E_x	P_{xt}
E_y	P_{yt}
E_z	P_{zt}
B_x	P_{yz}
B_y	P_{zx}
B_z	P_{xy}

4. Because of the cylindric symmetry of the problem, we will usually consider four (squared) components: electric longitudinal $\langle E_{\parallel}^2 \rangle = \langle E_z^2 \rangle$ and transverse $\langle E_{\perp}^2 \rangle = (\langle E_x^2 \rangle + \langle E_y^2 \rangle)/2$ and, respectively, magnetic longitudinal $\langle B_{\parallel}^2 \rangle = \langle B_z^2 \rangle$ and transverse $\langle B_{\perp}^2 \rangle = (\langle B_x^2 \rangle + \langle B_y^2 \rangle)/2$ (*cf.* Eq. (18)). For simplicity we use the notation $\langle\rangle$ instead of $\langle\rangle_{q\bar{q}} - \langle\rangle_{\text{vacuum}}$ as it was explained in Section 2.3, Eq. (19).

Fig. 1 illustrates the above points.

In this section we present the results obtained from the Monte Carlo simulations of the QCD with dynamical fermions. The details of the measurements were given in Section 2.4. Although we tried to exploit as much as possible the configurations which were available to us from the MT_c collaboration, the final results still have large statistical errors increasing rapidly with the size of the Wilson loop. Therefore, the range of the Wilson loops for which we are able to show reliable numbers is limited to 4×5. Also, the correlations have meaningful values only at small distances from the edges of the Wilson loop (in practice 2–3 lattice units). Nevertheless, the vicinity of the sources and the most interesting region between the quarks can be succesfully examined. It allows us to present first results with dynamical fermions obtained on the lattice of considerable size.

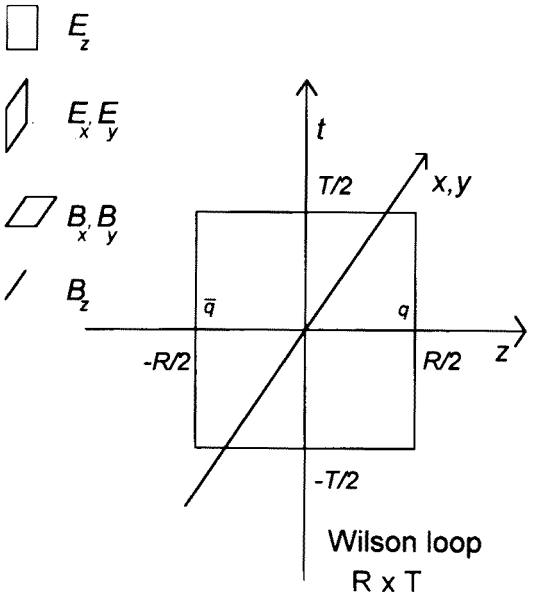

Fig. 1. The geometry of the measurements.

3.1. The shape of the flux tube and the distribution of particular components

First we analyse the relative importance of various components of the color fields. The following table summarizes the availability of the results for particular components. For greater loops the errors are comparable to, or larger, than the signal even in the region close to the loop.

component	$R_{\max}$	$T_{\max}$
$\langle E_{\parallel}^2 \rangle$	4	5
$\langle E_{\perp}^2 \rangle$	4	4
$\langle B_{\perp}^2 \rangle$	4	4
$\langle B_{\parallel}^2 \rangle$	3	3

Since the plaquettes are used to compute the values of particular components, we assume that the correlation value obtained from the Monte Carlo data represents the center of appropriate plaquette. Consequently, different components are measured on different sets of lattice points. In particular, no component can be measured at the "singular" sites where the quarks are located. Also, only the data for $\langle E_{\parallel}^2 \rangle$ is directly available exactly on the interquark line. Thus we will show the numbers from the vicinity of these sites. Interpolation will be used to construct the action and energy distributions in the whole space.

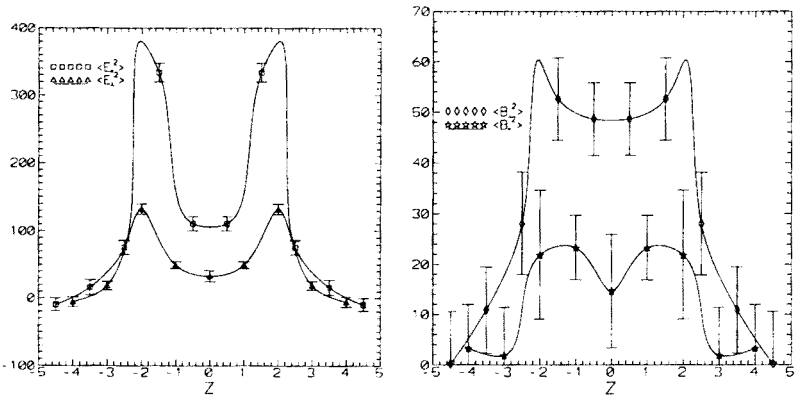

(a) (b)

Fig. 2. Longitudinal profiles for chromoelectric and chromomagnetic components

Fig. 2 summarizes the contributions of particular components for the 4×4 loop. The points denote values lying near the interquark axis. The general shape of the profiles supports quenched results first presented in [8] and [9], and then confirmed in many other papers: there is an evidence for the flux tube between the quarks visible in all components. Also, the general relationship between the absolute values of particular components is in agreement with previous results:

$$|\langle E_{\parallel}^2 \rangle| > |\langle E_{\perp}^2 \rangle| \geq |\langle B_{\perp}^2 \rangle| > |\langle B_{\parallel}^2 \rangle|, \tag{22}$$

which implies that the contribution of the chromoelectric components to the net flux between the quarks is dominant. We used absolute values in (22) since the measured magnetic components turn out to be negative: $\langle B_i^2 \rangle < 0$ (*cf.* Eq. (18) and (19)). This agrees with the quenched results, as well.

The dominance of $\langle E_{\perp}^2 \rangle$ over $\langle B_{\perp}^2 \rangle$ in Fig. 2 is connected with the different locations where these components are measured. For $\langle E_{\perp}^2 \rangle$ they were taken closer to the $t = T/2$ subspace (quark creation/annihilation time) which artificially increased the values (note that we use rather small Wilson loops). Also, the quenched results concerning transverse dependence of the components (*i.e.* perpendicularly to the z axis) [8–12] are reproduced in the case of dynamical fermions. This is shown in Fig. 3 for $\langle E_{\parallel}^2 \rangle$ and the loop $R = T = 3$. The data are taken at the middle time slice, for the z-slice mid-way between the quarks. The dependence is approximately exponential as also found in the quenched case [11]. We tried to fit our data to the combined exponential/gaussian dependence proposed in [13] using a

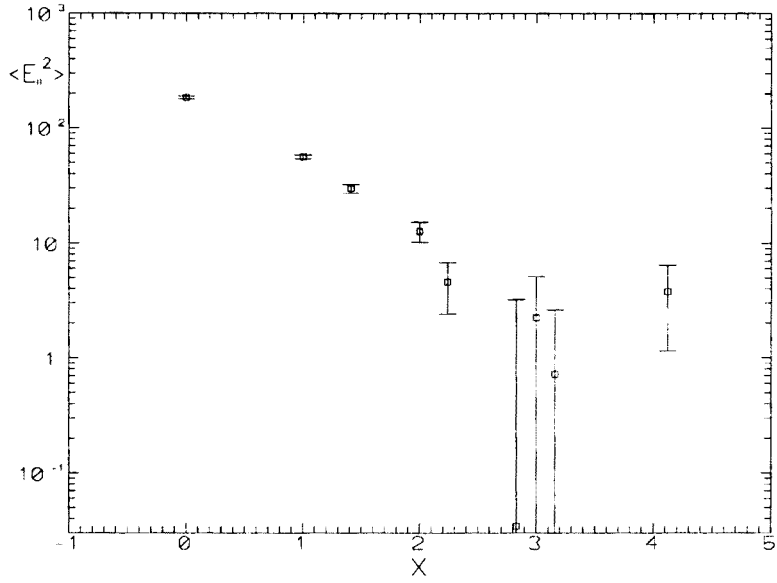

Fig. 3. Transverse profile for $\langle E_{\parallel}^2 \rangle$.

χ^2 fit but the result[3] clearly indicated the exponential rather than mixed dependence.

Now we turn to the energy and action density distributions which are two physical observables often used to describe the flux tube. They are given by

$$\varepsilon = \tfrac{1}{2}(E^2 + B^2), \tag{23}$$

$$\gamma = \tfrac{1}{2}(E^2 - B^2). \tag{24}$$

Since the magnetic contributions turned out to be negative, there is a strong cancellation between the two terms in (23) and the enhancement in (24). This was also found in earlier studies [11, 13, 14].

As we mentioned above, the values of particular components, as obtained from the measurements, are all defined at different space-time points. To compute the energy/action density distribution one has to combine them using interpolation. Many interpolating schemes are possible here (for example krigging, [13]). Since our data are concentrated in a relatively small volume around the quarks we have applied a simple method based on combined linear, polynomial and cubic spline interpolation. The raw results for

[3] We used MINUIT — the standard function minimization program available from the CERN Computer Centre Program Library

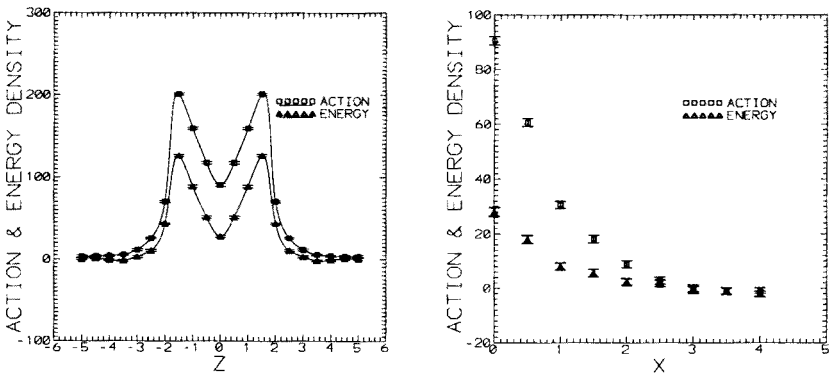

(a) (b)

Fig. 4. Energy and action density for the loop 3 × 3 — interpolated longitudinal and transverse profiles

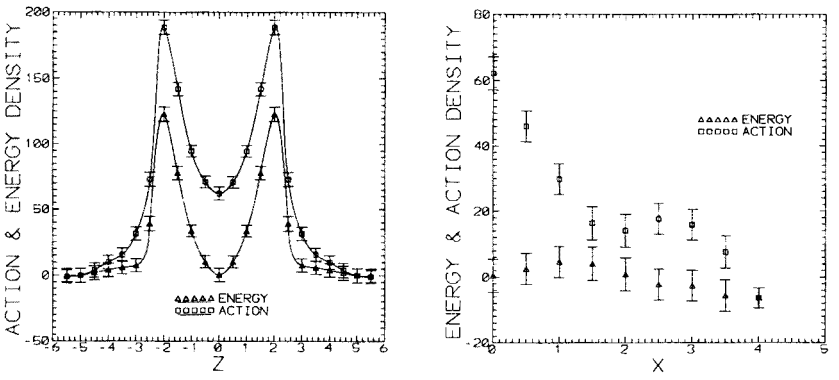

(a) (b)

Fig. 5. Energy and action density for the loop 4 × 4 — interpolated longitudinal and transverse profiles

each component have been first assigned to appropriate points of the finer lattice with the spacing $a' = a/2$, made of $16N_V$ sites, and then propagated to all remaining points of this lattice using the interpolation. Finally, all components have been combined giving the energy/action distribution on the fine lattice. The results for the Wilson loops 3 × 3 and 4 × 4 are presented in Figs 4 and 5, respectively. The lines were drawn for convenience and do not represent the results of the interpolation. As expected, the action density is significantly larger in the whole area around the quarks.

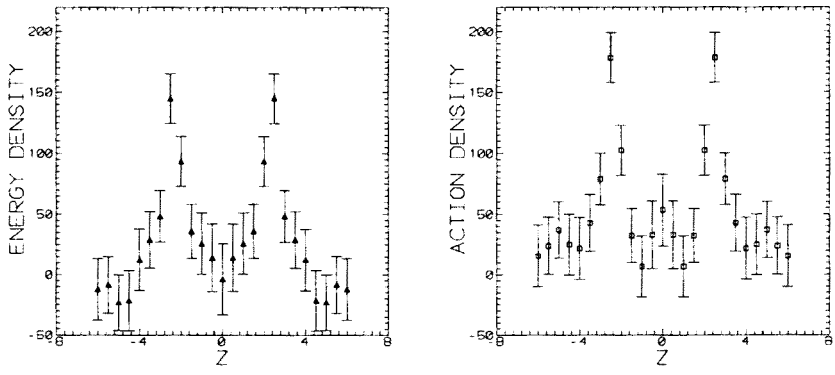

(a) (b)

Fig. 6. Energy and action density for the loop 5 × 5 — interpolated longitudinal profiles

Also, since the differences between the action and energy density measured in the peaks and in the mid-point between the quarks are nearly identical, we conclude that the chromoelectric component strongly dominates in the vicinity of the sources. It is not surprising since this region can be well described perturbatively and the perturbative fields close to the quarks are pure electric ones (compare the results of the analytic section).

To show how the results for energy and action profiles extrapolate to larger loops and how the statistical errors increase with the loop size we also present the data for $R = T = 5$. Although with significantly larger errors, the data in Fig. 6 coincide with the results obtained for smaller loops.

3.2. Comparison with quenched results

Now we proceed to the direct comparison of the longitudinal dependences for both the quenched approximation and the dynamical fermions case. This is done in Fig. 7 for the loop $R = T = 4$ and both chromoelectric components. The results for $\langle B_\perp^2 \rangle$ and $\langle B_\parallel^2 \rangle$ have much larger errors. To make the comparison more clear we have normalized our data forcing the values at the points labeled "N" to be the same as obtained from the quenched approximation. The data representing quenched results were taken from [11] [4]. The situation for electric components seems to be clear: including dynamical fermions results in lowering the value of the field in the area between the quarks making the tube weaker. This may be interpreted

[4] Although these reference results are for SU(2) we have chosen them since we had free access to all raw data which made the comparisons more reliable.

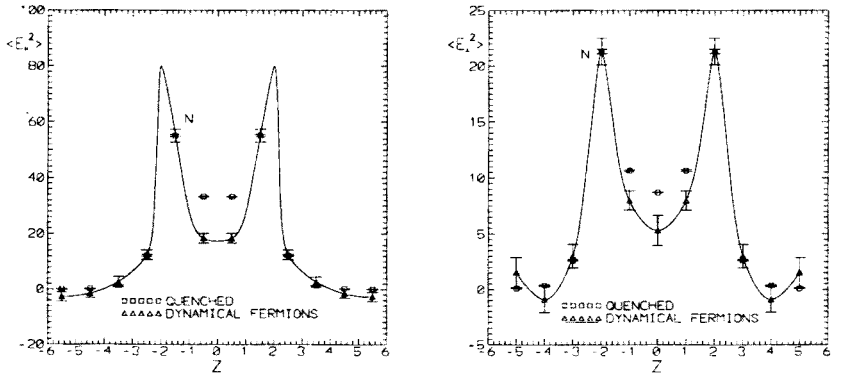

(a) (b)

Fig. 7. Quenched approximation vs. dynamical fermions: electric components, loop 4 × 4.

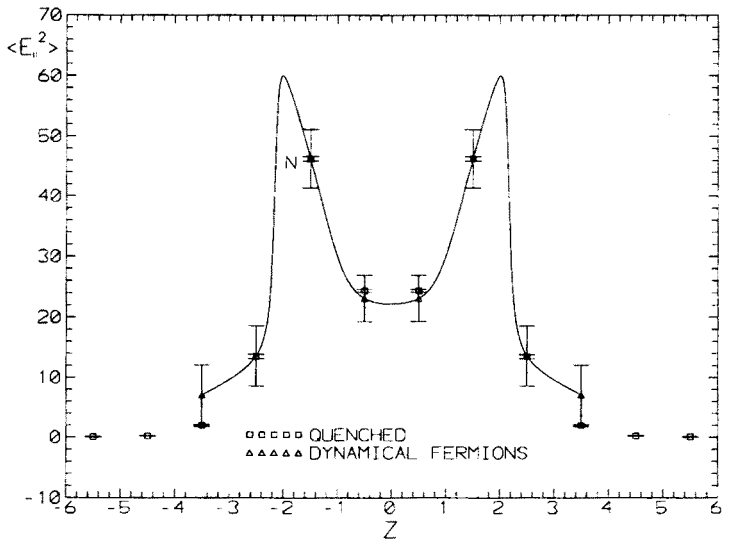

Fig. 8. Quenched approximation vs. dynamical fermions: $\langle E_{\parallel}^2 \rangle$, loop 4 × 5.

as an effect of entering the region where the flux tube can be broken. This phenomenon does not exist in the quenched approximation since in this case one neglects the important part of the strong interactions which takes part in breaking the tube, namely creation of light quarks.

Longitudinal profile of $\langle E_{\parallel}^2 \rangle$ for larger (4×5) loop is shown in Fig. 8. The effect of quenching is no longer visible although the errors are larger and the interpretation not so reliable.

The comparison of appropriate data for magnetic components is less conclusive because of much larger errors. Generally, no meaningful difference can be seen in this case between the (normalized) longitudinal profiles obtained in the quenched approximation and with dynamical fermions.

Also, as was mentioned previously, the transverse profiles for the components at $z = 0$, which we were able to measure with acceptable precision, show no significant qualitative difference compared to the quenched case.

3.3. The dependence on T

The average value of the color field component measured using the correlation (17) for any finite Wilson loop size is the mixture of the contributions from various quantum states of the gluon field with external sources $q\bar{q}$. Since we are mainly interested in revealing the shape of the flux tube in the lowest energy state, we have to increase the temporal extent of the loop T to supress the contributions from the excited states. However, as was mentioned above, the statistical quality of our results is acceptable only for small loops. With this in mind it is natural to ask, how well the flux data extrapolate to large T for various components.

To get an idea how important are higher states we first analyzed the dependence of the Wilson loop itself on its temporal extent[5].

Using the transfer matrix formalism the Wilson loop can be expanded in terms of consecutive energy states E_i of the lattice hamiltonian projected onto the $q\bar{q}$ sector of the Hilbert space [11]

$$\langle W(R,T) \rangle = \sum_i r_i \mathrm{e}^{-E_i(R)T}, \tag{25}$$

with the ground state energy E_0 equal to the static potential V_0.

For T large enough the lowest order term dominates the sum and one can rearrange the above equation to obtain following linear formula:

$$-\frac{1}{T} \ln \langle W(R,T) \rangle \simeq E_0(R) - \frac{1}{T} \ln r_0 \,. \tag{26}$$

This dependence is illustrated in Fig. 9 for various spatial extents of the loop. The squares represent the measured values and the straight lines

[5] The Wilson loops have been measured simultanously with the correlations as they form the denominator of Eq. (17). These measurements are much more precise than the ones for the components.

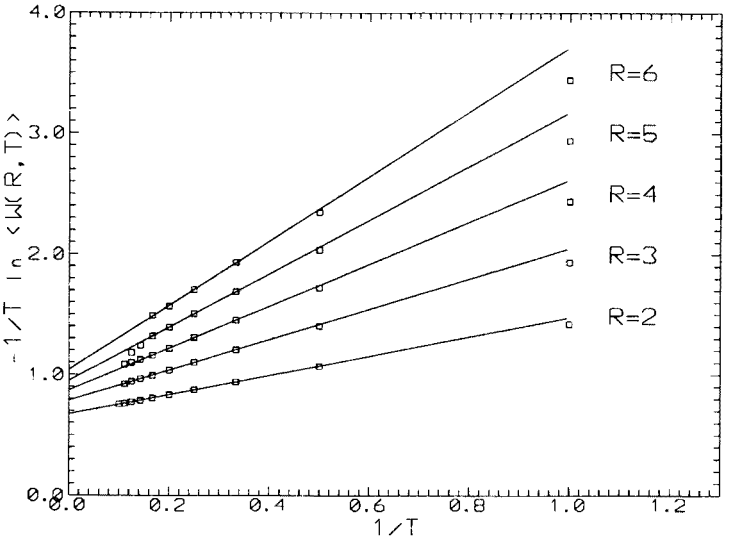

Fig. 9. The dependence of the Wilson loop on T.

— the fit to the linear formula given above. For $T \geq 3$ and $R \leq 4$ all the points lie on the fitted line indicating, that the contributions from the excited states can be neglected in this case and the series in (25) can be reduced to the first term. Generally, the smaller is the spatial extent of the loop, R, the smaller is the deviation from the linear formula (26).

The dependence of the correlations (17) on T is shown in Fig. 10. The values were taken from the middle of the Wilson loop (the mid-point between the quarks and the middle time slice). Where it was possible, the results were presented for various spatial extents, R.

The results for $R = 2$ may indicate, that the values stabilize for $T \geq 3$ which means that there is no need for going to very large loops to obtain reliable results, at least for small spatial extents. This coincides with the conclusion we came to examining the T dependence of the Wilson loops. Unfortunately, we cannot state the same for larger R. However, since the best results for $R = 2$, $\langle E_{||}^2 \rangle$ are comparable to the quenched ones, we hope that also for other components higher states do not contribute substantially, as it was obtained in the quenched case [11].

Another interesting information contained in our results concerns the lattice energy/action sum rules developed by Michael [14]. We tried to compare our results to the ones evaluated according to the sum rules.

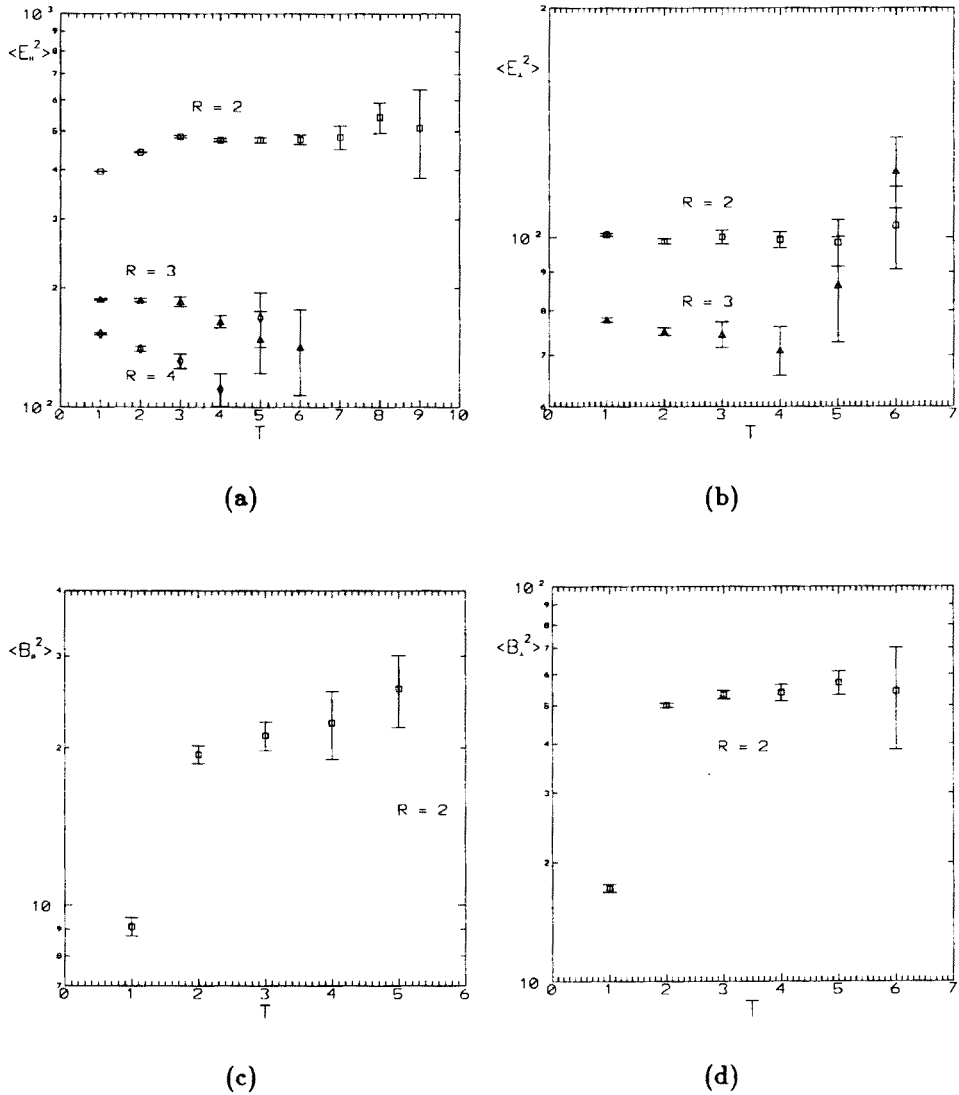

Fig. 10. The dependence of various components on T.

Energy

The Michael energy sum rule for the quenched case reads [14]

$$\tfrac{1}{2}a^3 \sum_{\vec{x}} \left(E(\vec{x})^2 + B(\vec{x})^2\right) = E_0(R)\,, \tag{27}$$

where the sum should be computed in the lowest quantum state of the color field. This formula expresses the simple fact that the energy required to pull

the quarks apart (the potential) can be obtained by integrating the energy density over all space. The potential $E_0(R)$ can be obtained from Eq. (26) and Fig. 9.

The curves in Fig. 11 show the energy density integrated over the increasing cuboidal volume surrounding the Wilson loop, for $R = 3$ and $T = 3$ and $T = 5$. This volume is represented by the distance d of the faces of the cuboid from the edges of the loop (equal in all directions). The errors grow with T as expected from previous results. Also, since the errors of the field values increase with the distance from the Wilson loop, the error bars increase with d. The values for $T = 3$ have small errors and clearly stabilizate at $E(d = 4) = 3.84(0.16)$ which means that in this case the whole energy is concentrated in the volume $(R + 8) \times 8 \times 8$. Unfortunately, this rather precise value cannot represent the left side of (27) since it probably contains significant contributions from higher states. Thus we turn to the line $T = 5$ which seems to stabilizate at $E(d = 3) = 2.48(0.56)$ showing that the lowest state energy is concentrated in smaller volume around the sources. Appropriate value for the potential obtained from the data plotted in Fig. 9 is $E_0(R = 3) = 7.87$ with negligible error. This discrepancy results from neglecting the important contribution to the energy density originating from the quark condensate [23]. Our results show that this additional contribution is comparable to the gluonic one. This is in contrast with the quenched case where the sum rule (27) is rather well satisfied [11, 12].

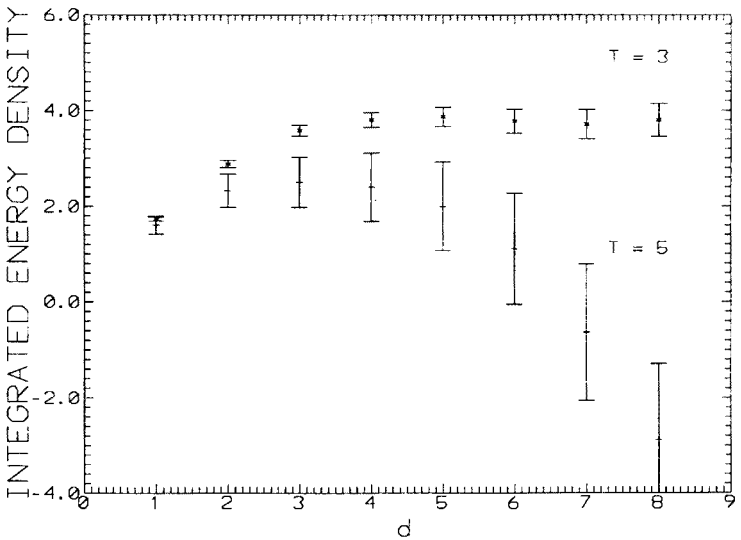

Fig. 11. Integration of the energy density over the increasing volume for $R = 3$.

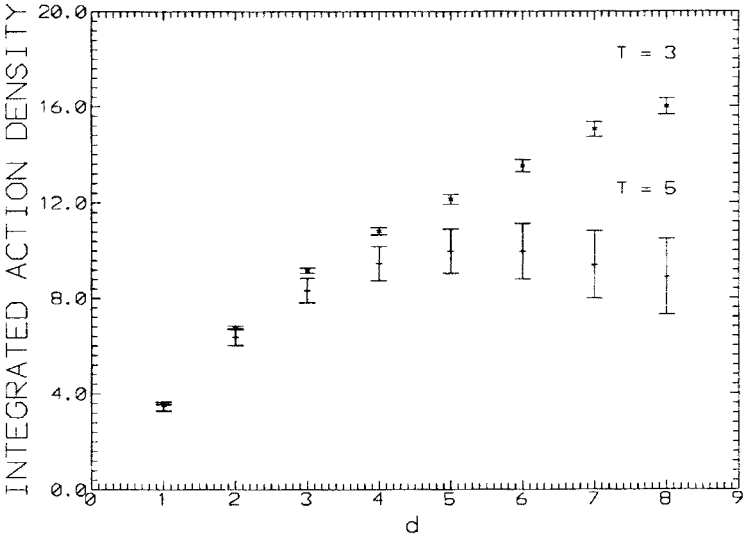

Fig. 12. Integration of the action density over the increasing volume for $R = 3$.

Action

The action sum rule without dynamical fermions reads [14]

$$\tfrac{1}{2}a^3 \sum_{\vec{x}} \left(E(\vec{x})^2 - B(\vec{x})^2\right) = -\beta \frac{\partial \ln a}{\partial \beta} \left(E_0(R) - \frac{f(\beta)}{a}\right) - \frac{\beta}{a}\frac{\partial f(\beta)}{\partial \beta}, \quad (28)$$

where $f(\beta)/a$ denotes the self-energy contribution.

Appropriate results are presented in Fig. 12. For $T = 3$ the action extends over a large region around the Wilson loop (much larger than for energy density, as expected). For $T = 5$, which is more suitable for our purpose, the action fills the volume $(R + 10) \times 10 \times 10$. Its total value is 10.00(0.96) which is about 4 times larger than the integrated energy. This is considerably less than found in the quenched case where the action density is larger by the factor (7–9) than the corresponding energy density [12]. This difference may again be a result of neglecting the quark condensate part of the action density. Another possible contribution to this difference may come from the self-energy terms of Eq. (28) which, for small values of R examined in our measurements, are more important.

3.4. Integral method

We have also checked an alternative method of measuring the components of $F_{\mu\nu}(x)$ in the lowest quantum state, suggested to us by R. Sommer.

We will call it the *integral method.* Similar methods were also used for other purposes [26].

We consider the dependence of the sum

$$S_{\mu\nu}(\vec{x}) = \sum_{0 \le t \le T} f_{\mu\nu}(\vec{x}, t) \tag{29}$$

on T. There can be substantial contributions from higher quantum states of the $q\bar{q}$ pair to this sum as a signal from the creation/annihilation moments, especially in the vicinity of the edges, $\pm T/2$, but the lowest state contributes equally for each t. Consequently, we expect the asymptotically linear dependence

$$S(\vec{x}, T) = a(\vec{x}) + b(\vec{x})T\,, \tag{30}$$

with $b(\vec{x})$ being the ground state contribution.

More formally, using transfer matrix $\mathcal{T}$ formalism on the lattice with the time extent N_t and denoting the quark creation/annihilation operators by $\hat{S}$ and the plaquette operator by $\hat{P}$ we can express the correlation $\langle WP \rangle$ as

$$\langle WP(\vec{x}, t) \rangle = Z^{-1} \mathrm{Tr} \left(\mathcal{T}^{N_t - T} \hat{S} \mathcal{T}^{t}_{q\bar{q}} \hat{P} \mathcal{T}^{T-t}_{q\bar{q}} \hat{S} \right) . \tag{31}$$

Using appropriate formulas for $\langle W \rangle$ and $\langle P \rangle$, evaluating the traces and putting the results into Eq. (17) we obtain for any $f_{\mu\nu}$ an infinite series involving all eigenvalues of the transfer matrix. Leaving only the dominant terms depending on two lowest energy contributions we can write

$$f(t) \simeq F_0 + A\left(\frac{\Lambda_1}{\Lambda_0}\right)^t + B\left(\frac{\Lambda_1}{\Lambda_0}\right)^{T-t} - C\left(\frac{\Lambda_1}{\Lambda_0}\right)^T , \tag{32}$$

where Λ_i is the i-th eigenvalue of the transfer matrix in the $q\bar{q}$ sector, $\Lambda_i = \mathrm{e}^{-E_i}$, and F_0, A, B, C are constants independent of T (F_0 is the true ground state value of the component). The sum over t now takes the form

$$S(\vec{x}, T) = (A + B) \frac{1 - \left(\frac{\Lambda_1}{\Lambda_0}\right)^T}{1 - \left(\frac{\Lambda_1}{\Lambda_0}\right)} + \left(F_0 - C\left(\frac{\Lambda_1}{\Lambda_0}\right)^T \right) T \tag{33}$$

which, for T large enough, becomes (30).

Generally, the results obtained using the integral method are in agreement with the ones presented previously. The errors of the linear fits to (30) are also comparable with the standard ones. Fig. 13 presents an example of the longitudinal profile obtained using this method for $R = 4$. It is compared to the profile from Fig. 2 computed near the middle time

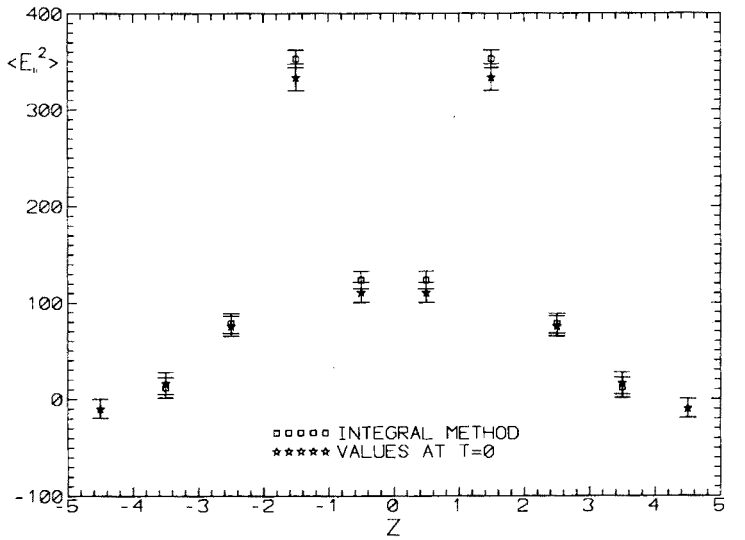

Fig. 13. Longitudinal profile for $\langle E_{\parallel}^2 \rangle$, $R = 4$ obtained with the integral method.

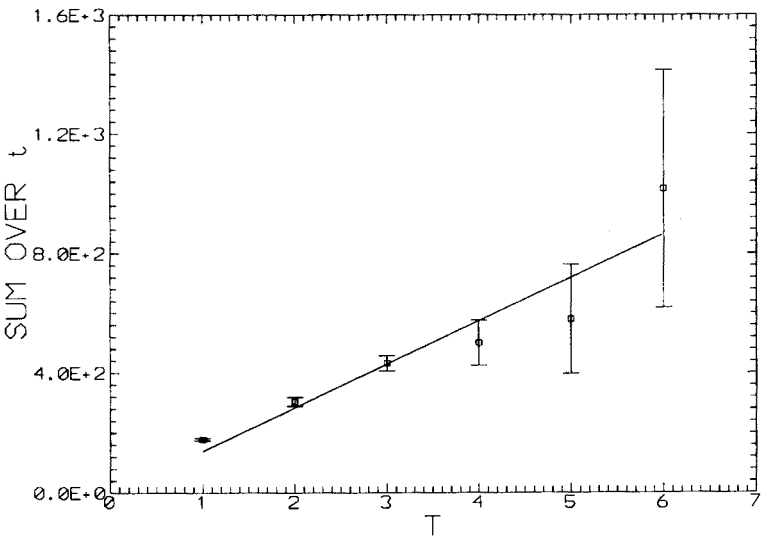

Fig. 14. The illustration of the linear dependence $S(T)$ for the space point $z = 2.5$.

slice $T = 0$. In this case the errors of the integral method are even a little smaller. Fig. 14 is an illustration of the linear dependence given by Eq. (30) for one of the points of Fig. 13.

This method can be an interesting alternative to the standard one since it automatically involves higher degree of averaging by combining the data for variuos T. In the standard method the same result can be achieved by fitting the parameters to the sum of exponents, which is more difficult.

3.5. Summary of the MC results

To summarize the Monte Carlo section of this work we point out the most important results:

1. Generally, the results obtained using dynamical fermions coincide with the previous, quenched ones. This concerns the shape of the flux tube (longitudinal and transverse profiles of the components, energy and action), the relationship between various components and their dependence on T.
2. The inclusion of dynamical fermions significantly lowers the value of the color field in the region between the quarks. This effect may be interpreted as entering the range of interquark distances where breaking the flux tube can be observed.
3. The check of the energy and action sum rules applied to our results clearly indicates, that another important contribution of the flux tube must be taken into account, namely the quark condensate.
4. The alternative method of computing the lowest state values of the components has been introduced. It produces results consistent with the ones obtained in the standard way.

4. Color fields around static quarks in the weak coupling limit

4.1. Action in the weak coupling limit

As it was mentioned above lattice QCD can be treated as just another method of regularization of the continuous Yang–Mills theory. In the weak coupling approximation, which is the perturbative limit of the lattice theory, all results of other regularization schemes (Pauli–Villars regularization, dimensional regularization) can be reproduced. However, lattice regularization is less convenient and, in practice, extensive weak coupling calculations are carried out less frequently than in other schemes.

In our work we perform the weak coupling calculations mainly to better understand the physics of the Monte Carlo results. In general we expect, that nonperturbative effects will modify the distribution of the color fields but we have no idea, how significant this modification will be, especially at larger distances from the charges. In the vicinity of the sources the Coulomb component of the interaction probably dominates and perturbative results

can be quite meaningful. Also the comparison of perturbative QCD results with the classical electric dipole is interesting.

The Wilson action

In the weak coupling domain the link variable can be approximated by its power series and (1) yields

$$U_l = 1 + gA_l + \tfrac{1}{2}g^2 A_l^2 + \dots . \tag{34}$$

The lattice constant a was absorbed into the gauge field A and we have defined $g \equiv ig_0$.

Using this formula one can expand the plaquette (Appendix B) and the Wilson action (2) to obtain

$$S^{\mathrm{W}} = S_0^{\mathrm{W}} + gS_1^{\mathrm{W}} + g^2 S_2^{\mathrm{W}} + O(g^3) . \tag{35}$$

Detailed expressions for all these terms are listed in Appendix C.

The gauge fixing term and the counterterm

The terms in Eq. (35) are not the only ones that we must take into account. Following the Faddeev–Popov quantization technique [40] we should include terms which prevent the Feynman integration over gauge fields which are connected by a gauge transformation. These terms result from factoring out a path integral over gauge transformations. Appropriate procedure on the lattice was outlined by Wilson [5] and carried out by Baaquie [41]. First, the gauge fixing term is introduced which reduces the lattice theory to the conventional discretized field theory in which the field variables $A_\mu(x)$ take values over an infinite range $(-\infty, +\infty)$ and the Feynman amplitude is definite. This modification requires introduction of the counterterm so that the amplitude remains unchanged.

The action now takes the form

$$S' = S + S^{\mathrm{GF}} + S^{\mathrm{FP}}, \tag{36}$$

where S^{GF} is the gauge-fixing term and S^{FP} — the counterterm.

Denoting the gauge transformation on the lattice by

$$U_\mu^{(V)}(x) = V(x)U_\mu(x)V^\dagger(x+\mu) \tag{37}$$

and defining the counterterm to be

$$\exp\left(S^{\mathrm{FP}}(U)\right) = \frac{1}{\int[\mathrm{d}V]\exp\left(S^{\mathrm{GF}}(U^{(V)})\right)} , \tag{38}$$

(we temporarily neglect g) one can show that [41]

$$Z = \int [\mathrm{d}U] \mathrm{e}^{S} = \int [\mathrm{d}U] \mathrm{e}^{S'}. \tag{39}$$

For the specific gauge-fixing term

$$\exp\left(S^{\mathrm{GF}}(A)\right) = \prod_{x,a} \delta\left(\sum_{\mu} \Delta_{\mu} A^{a}_{\mu}(x-\mu) - t^{a}(x)\right), \tag{40}$$

where $t^{a}(x)$ are fixed numbers, one can evaluate appropriate S^{FP}

$$\exp\left(S^{\mathrm{FP}}(A)\right) = \det\left(d\left(1 + \frac{1}{d}M + \frac{1}{d}L\right)\right), \tag{41}$$

with the matrices $d(k), M^{ad}(k,q)$ and $L^{ad}(k,q)$:

$$d(k) = \begin{cases} 1 & \text{if } k = 0, \\ \sum_{\mu} |1 - \mathrm{e}^{ik_{\mu}}|^{2} & \text{if } k \neq 0 \end{cases}$$

(diagonal),

$$M^{ad}(k,q) = \tfrac{1}{2} f^{abd} \sum_{\mu} (1 - \mathrm{e}^{-ik_{\mu}})(1 + \mathrm{e}^{iq_{\mu}}) A^{b}_{\mu}(k-q) \tag{42}$$

and

$$L^{ad}(k,q) = \tfrac{1}{12} f^{abe} f^{cde} \sum_{k'} \sum_{\mu} (1 - \mathrm{e}^{-ik_{\mu}})(1 - \mathrm{e}^{iq_{\mu}}) A^{b}_{\mu}(k-k'-q) A^{c}_{\mu}(k'), \tag{43}$$

respectively [41].

Using $\det X = \exp(\mathrm{Tr} \ln X)$ and taking into account the terms quadratic in A we can transform (41) to the form given in Appendix C, Eq. (109). In continuous QCD the Faddeev–Popov ghosts are introduced in this place to express S^{FP}.

The measure term

Finally, to perform the SU(3) integration, we have to include the measure term according to

$$\int \mathrm{d}g f(g) = \int \mathrm{d}\alpha_1 \ldots \mathrm{d}\alpha_n J(\alpha) f(g(\alpha)), \tag{44}$$

where g is the group element, α — the parameters of the group and J — the Jacobian which can be evaluated from the following formula [4]

$$J(\gamma) \simeq \det{}^{-1} \left. \frac{\partial(\alpha(\beta,\gamma))}{\partial\beta} \right|_{\beta=\beta(e)} \tag{45}$$

assuming that the (composite) parameters α, β, γ are connected by the group multiplication

$$g(\alpha(\beta,\gamma)) = g(\beta)g(\gamma). \tag{46}$$

For $U = \exp(iA^aT^a)$ we can express the Jacobian as the exponent of the measure term which gives

$$\prod_{x,\mu} \mathrm{d}U_\mu(x) = \exp(-S^M) \prod_{x,\mu,a} \mathrm{d}A^a_\mu(x)\,. \tag{47}$$

S^M is given in Appendix C.

Collecting above formulas we express the weak coupling action in the form

$$S = S_0 + gS_1 + g^2S_2 + O(g_0^3), \tag{48}$$

where

$$S_0 = S_0^{\mathrm{W}} + S_0^{\mathrm{GF}}, \tag{49}$$

the first order term receives contribution only from the Wilson action

$$S_1 = S_1^{\mathrm{W}} \tag{50}$$

and the Wilson action, measure and Faddeev–Popov terms contribute to the second order

$$S_2 = S_2^{\mathrm{W}} + S_2^{\mathrm{M}} + S_2^{\mathrm{FP}}. \tag{51}$$

4.2. Perturbative calculations of the $\langle WP \rangle$ correlations in the lowest order (tree approximation)

We are to compute the $\langle WP \rangle$ correlations in the weak coupling approximation *i.e.* assuming small value of the bare coupling constant g [42]. As earlier the formula (17) will be our starting point.

Let us start with the power expansion of the Wilson loop. Using (34) and (4) one can write

$$W = 1 + g^2w_2 + g^3w_3 + g^4w_4 + O(g^5). \tag{52}$$

Note that there is no first order term in this formula due to the trace in the definition of the Wilson loop.

The same holds for the plaquette P (Wilson loop of the size 1×1) with appropriate coefficients p_i. They are given in Appendix B. Taking the average we obtain for the main terms in (17)

$$\langle W \rangle = 1 + g^2\langle w_2 \rangle + g^3\langle w_3 \rangle + g^4\langle w_4 \rangle + O(g^5), \tag{53}$$

and

$$\begin{aligned}\langle WP \rangle^c =& g^4\langle w_2 p_2 \rangle^c \\ &+ g^5\left(\langle w_2 p_3 \rangle^c + \langle w_3 p_2 \rangle^c\right) \\ &+ g^6\left(\langle w_2 p_4 \rangle^c + \langle w_3 p_3 \rangle^c + \langle w_4 p_2 \rangle^c\right),\end{aligned} \tag{54}$$

where $\langle\rangle^c$ denotes the *connected* correlation

$$\langle XY \rangle^c = \langle XY \rangle - \langle X \rangle\langle Y \rangle. \tag{55}$$

Since the average denoted by $\langle\rangle$ involves the full weak coupling action, the $\langle w_i p_j \rangle^c$ terms are still g-dependent. To express them in terms of free propagators we introduce the following definitions

$$\langle X \rangle_0 = \frac{\int X \mathrm{e}^{S_0}}{\int \mathrm{e}^{S_0}}, \tag{56}$$

$$\langle X \rangle = \frac{\int X \mathrm{e}^{S}}{\int \mathrm{e}^{S}}. \tag{57}$$

Now one can easily obtain (using (48) and expanding the exponents)

$$\langle X \rangle = X^{(0)} + gX^{(1)} + g^2X^{(2)} + O(g^3), \tag{58}$$

and

$$X^{(0)} = \langle X \rangle_0, \tag{59}$$

$$X^{(1)} = \langle X S_1 \rangle_0^c, \tag{60}$$

$$X^{(2)} = \langle X \tilde{S}_2 \rangle_0^c - \langle X S_1 \rangle_0^c \langle S_1 \rangle_0, \tag{61}$$

with

$$\tilde{S}_2 = \tfrac{1}{2}S_1^2 + S_2. \tag{62}$$

Defining

$$\rho_{ij} = \langle w_i p_j \rangle^c \tag{63}$$

and expanding it according to (58)

$$\rho_{ij} = \rho_{ij}^{(0)} + g\rho_{ij}^{(1)} + g^2\rho_{ij}^{(2)} + O(g^3)\,, \tag{64}$$

one has

$$\rho_{ij}^{(0)} = \langle w_i p_j \rangle_0^{\mathrm{c}}\,, \tag{65}$$

$$\rho_{ij}^{(1)} = \langle w_i p_j S_1 \rangle_0 - \langle w_i \rangle_0 \langle p_j S_1 \rangle_0 - \langle p_j \rangle_0 \langle w_i S_1 \rangle_0 \tag{66}$$

and

$$\rho_{ij}^{(2)} = \langle (w_i p_j)\, \tilde{S}_2 \rangle_0^{\mathrm{c}} - \langle w_i \rangle_0 \langle p_j \tilde{S}_2 \rangle_0^{\mathrm{c}} - \langle p_j \rangle_0 \langle w_i \tilde{S}_2 \rangle_0^{\mathrm{c}} + \langle w_i S_1 \rangle_0 \langle p_j S_1 \rangle_0\,. \tag{67}$$

These equations were already simplified using the fact that $S_1 \sim AAA$ and

$$\langle A_1 A_2 \ldots A_{2k-1} \rangle_0 = 0\,. \tag{68}$$

The correlation to be computed, Eq. (17) now takes the form

$$f(x) = \frac{\beta}{a^4} \frac{g^4\tilde{\rho}_4 + g^5\tilde{\rho}_5 + g^6\tilde{\rho}_6 + O(g^7)}{1 + g^2 w_2^{(0)} + O(g^3)}\,, \tag{69}$$

where the indices $\mu\nu$ have been suppressed and

$$\tilde{\rho}_4 = \rho_{22}^{(0)}\,, \tag{70}$$

$$\tilde{\rho}_5 = \rho_{23}^{(0)} + \rho_{32}^{(0)} + \rho_{22}^{(1)}\,, \tag{71}$$

$$\tilde{\rho}_6 = \rho_{24}^{(0)} + \rho_{42}^{(0)} + \rho_{33}^{(0)} + \rho_{23}^{(1)} + \rho_{32}^{(1)} + \rho_{22}^{(2)}\,. \tag{72}$$

Thus the first nonvanishing coefficient of the series

$$f = \frac{\beta}{a^4}\left(f_0 + g f_1 + g^2 f_2 + \ldots\right) \tag{73}$$

is

$$f_4 = \rho_{22}^{(0)} = \langle w_2 p_2 \rangle_0^{\mathrm{c}}\,. \tag{74}$$

Using the expression (90) for w_2 given in Appendix B and reducing internal propagators in W and P

$$\langle (A_l A_m)(A_{l'} A_{m'}) \rangle_0^{\mathrm{c}} = \langle A_l A_{l'} \rangle_0 \langle A_m A_{m'} \rangle_0 + \langle A_l A_{m'} \rangle_0 \langle A_m A_{l'} \rangle_0\,, \tag{75}$$

where $l, m \in W$ and $l', m' \in P$, Eq. (74) can be rewritten as

$$f_4 = \frac{1}{8n^2} \sum_{\substack{lm \in W \\ l'm' \in P}} \langle A_l^a A_{l'}^{a'} \rangle \langle A_m^a A_{m'}^{a'} \rangle = \frac{n_g}{8n^2} \sum_{\substack{lm \in W \\ l'm' \in P}} D_{ll'} D_{mm'} . \tag{76}$$

It is the final form of the tree approximation of the correlation between Wilson loop and plaquette on a lattice, which has been directly used in computer calculations. $D_{ll'}$ denotes the (free) propagator between the links l, l' and n_g is the number of gluons of the theory (8 in case of SU(3)).

First order calculations have been implemented in FORTRAN and performed in 1992–1993 on the IBM Risc workstation in the Particles Theory Department. The method uses configuration space instead of momentum one and is quite effective since the propagators for particular lattice can be computed once (using Fast Fourier Transform, Appendix A) and then reused for various Wilson loops and the positions/orientations of the plaquette.

4.3. Next order (one loop) terms

Next two coefficients of the series (73) produced by (69) are

$$f_5 = \rho_{23}^{(0)} + \rho_{32}^{(0)} + \rho_{22}^{(1)} \tag{77}$$

and

$$f_6 = -w_2^{(0)} \rho_{22}^{(0)} + \rho_{24}^{(0)} + \rho_{42}^{(0)} + \rho_{33}^{(0)} + \rho_{23}^{(1)} + \rho_{32}^{(1)} + \rho_{22}^{(2)} . \tag{78}$$

Taking into account that $w_i \sim A \ldots A$ with i As (Appendix B) and $S_1 \sim AAA$ we obtain from (65)–(67) and (68)

$$f_5 = 0 \tag{79}$$

and the terms of f_6 are

$$w_2^{(0)} = \langle w_2 \rangle_0 , \tag{80}$$

$$\rho_{22}^{(0)} = \langle w_2 p_2 \rangle_0^{\mathrm{c}} , \tag{81}$$

$$\rho_{24}^{(0)} = \langle w_2 p_4 \rangle_0^{\mathrm{c}} , \quad \rho_{42}^{(0)} = \langle w_4 p_2 \rangle_0^{\mathrm{c}} , \quad \rho_{33}^{(0)} = \langle w_3 p_3 \rangle_0 , \tag{82}$$

$$\rho_{23}^{(1)} = \langle w_2 p_3 S_1 \rangle_0 - \langle w_2 \rangle_0 \langle p_3 S_1 \rangle_0 ,$$

$$\rho_{32}^{(1)} = \langle w_3 p_2 S_1 \rangle_0 - \langle p_2 \rangle_0 \langle w_3 S_1 \rangle_0 , \tag{83}$$

and

$$\rho_{22}^{(2)} = \langle (w_2 p_2) \tilde{S}_2 \rangle_0^{\mathrm{c}} - \langle w_2 \rangle_0 \langle p_2 \tilde{S}_2 \rangle_0^{\mathrm{c}} - \langle p_2 \rangle_0 \langle w_2 \tilde{S}_2 \rangle_0^{\mathrm{c}} . \tag{84}$$

Equations (80)–(84) constitute the second order (one loop) approximation of the correlation coefficient between Wilson loop and plaquette.

Corresponding propagator expansions analogous to Eq. (76) are given in Appendix D.

Appropriate calculations have been carried out in configuration space using a C program being the extension of the earlier one written in FORTRAN for the tree computations. The C language preprocessor was especially useful with its ability to define parametrized macros representing rather complicated computational formulas and lattice objects without slowing down the computations [43]. The configuration space and FFT were used as before (Appendix A).

During the one loop computations it was essential to use the double precision arithmetic to obtain reliable results, especially for the terms with many nonzero couplings like in the case of $\langle E_{\|}^2 \rangle$ (*cf.* Appendix D).

5. Perturbative results

In this section we present analytic results concerning the distribution of the color fields around static charges. The method and used formulas have been explained in section 4 and in the appendices.

We have performed part of the computations on a $17^3 \times 20$ lattice to preserve the possibility of direct comparison with the MC data produced by the Cracow–LSU collaboration (high statistical quality of these results allows for comparisons using much larger Wilson loops than it is available from our MC data) [11]. We have also set the value of β to be 2.4 and $a = 0.1285$ as for these reference data. Results from much bigger lattice, *i.e.* 32^4, were also obtained to reveal the details of the distribution. All these computations were performed only in the tree approximation.

We also present the results of the one loop calculations. However, in this case, the size of the lattice and the range of Wilson loops were limited to significantly smaller values because of numerical complexity and time requirements of the program. In these calculations we mainly concentrated on the importance of one loop order terms and on qualitative changes introduced in this order.

All weak coupling calculations presented in following sections were carried out for the SU(3) gauge group.

5.1. Fields around quarks in the tree approximation — general picture

We begin with some comments implied by the geometry of the problem. As we expect from (76), the $\langle B_{\|}^2 \rangle$ connected with plaquettes in plane xy vanishes in the whole space-time (note the presence of $\delta_{\mu\nu}$ in (88), *cf.* Appendix A). Furthermore, both $\langle B_x^2 \rangle$ and $\langle B_y^2 \rangle$ vanish in the subspace

$t = 0$. To see it, one can imagine appropriate plaquette lying perpendicularly to the Wilson loop in the same distance from its upper and lower space sides and consider all possible combinations of the signs in (76). The same observation is true for both $\langle E_x^2 \rangle$ and $\langle E_y^2 \rangle$ which, in turn, are equal to zero if $z = 0$. In contrast to $\langle B_{\|}^2 \rangle$, which in the lowest order has no coupling to the Wilson loop at all, $\langle E_{\|}^2 \rangle$ has the strongest one. It is connected with the fact that appropriate plaquette and the Wilson loop are parallel. In consequence, the number of the nonzero products of the propagators in (76) is relatively large.

These facts result only from the symmetry of the problem and provide consistency check of the numerical computations. They are in agreement with the usual interpretation of the Wilson loop as representing the world line of the static $q\bar{q}$ pair which, in the Born approximation, reduces to the simple electric dipole.

Further results are presented in the following figures. Note: squares, stars *etc.* represent exact, discrete values produced by the program. All curves were fitted using slightly modified spline interpolation. Their purpose is to distinguish and clarify particular dependencies.

Main results concerning the distribution of the fields around quarks are presented in Figs. 15–17. They have been computed on the 32^4 lattice for the the Wilson loop of the size $R = 8, T = 11$. These results serve mainly as a check of consistency with our expectations based on classical Maxwell electrodynamics.

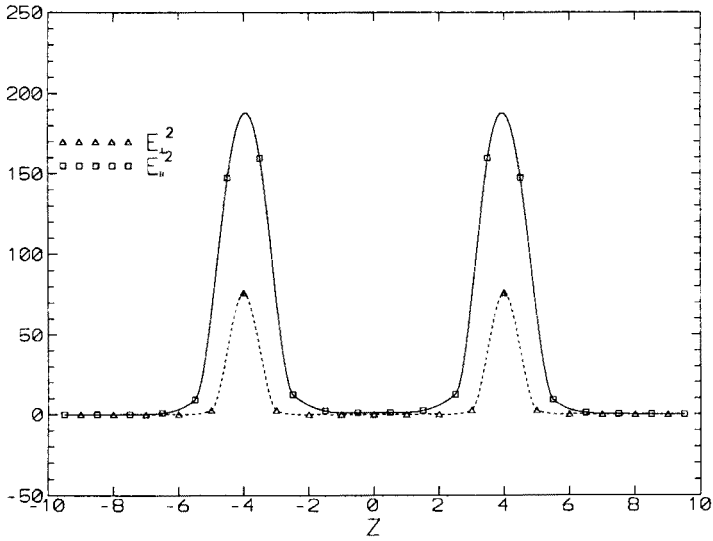

Fig. 15. Longitudinal profiles for $\langle E_{\|}^2 \rangle$ and $\langle E_{\perp}^2 \rangle$.

Fig. 15 shows typical longitudinal profiles, for $t = 0$, obtained for the electric longitudinal (stars) and transverse (squares) components. All these profiles are presented for loops with odd T. It guarantees that the values represent exactly the middle time – slice. The classical electrodynamic expectation for $\langle E_\perp^2 \rangle$ exactly on the z axis is zero (only longitudinal field exists on a line connecting the charges for the classical electric dipole). Since we are not able to obtain appropriate values directly on this axis[6] we cannot state that our lattice results break this obvious symmetry. Instead, as it is shown in Fig. 16, natural extrapolation to $x = y = 0$ can be proposed, which supports it.

The shape of both energy and action distribution exactly on the $q\overline{q}$ axis is the same as the one given in Fig. 15 for $\langle E_\parallel^2 \rangle$ due to vanishing of $\langle E_\perp^2 \rangle$ and $\langle B^2 \rangle$. Fig. 15 presents also the most apparent difference between perturbative and Monte Carlo results: there is practically no field in a large region between quarks *i.e.* no flux tube, responsible for confinement. This issue will be discussed below. As was mentioned above there are no magnetic fields for the timeslice $t = 0$.

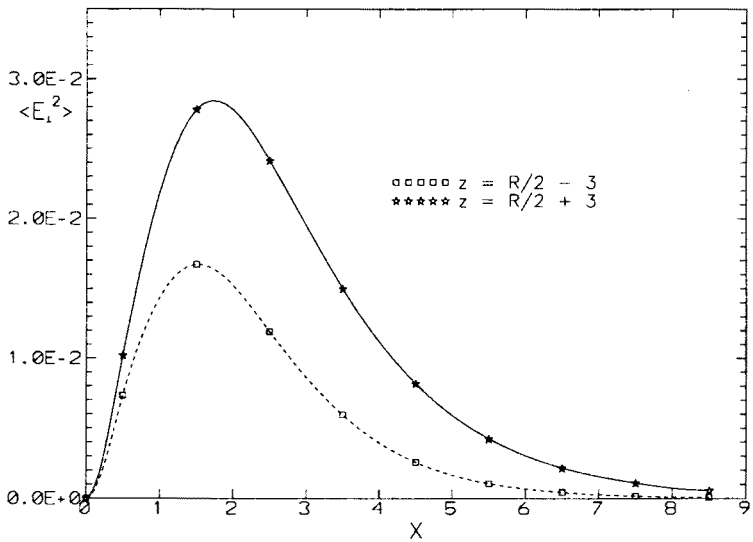

Fig. 16. Transverse dependence for $\langle E_\perp^2 \rangle$ and two different z.

Fig. 16 shows the transverse dependence of $\langle E_\perp^2 \rangle$ for $z = R/2 \pm 3$. Stars represent $R/2 + 3$ (the point outside the dipole) and squares $R/2 - 3$ (the

[6] This problem was discussed in sections covering Monte Carlo results

point between the charges, a little closer to one of them) [7]. The zero value on the interquark line was forced artificially to meet our classical expectation (it seems not to be very artificial looking at the program output points) . The dashed line lies lower as there is much stronger compensative influence of the quark at $z = -R/2$. Both curves have clear maxima, like appropriate transverse dependences for classical electric dipole do, and the maximum for the dashed line (inside the dipole) lies closer to the interquark line than that for the solid line. This agrees qualitatively with the appropriate classical relation: $x_{max} = 1.83$ for the profile at $z = R/2 - 3$ and $x_{max} = 2.12$ for $z = R/2 + 3$ in some units. It contrasts with the nonperturbative case, where generally fields are stronger between the charges as a result of the flux tube formation and there are no other maxima outside the interquark line.

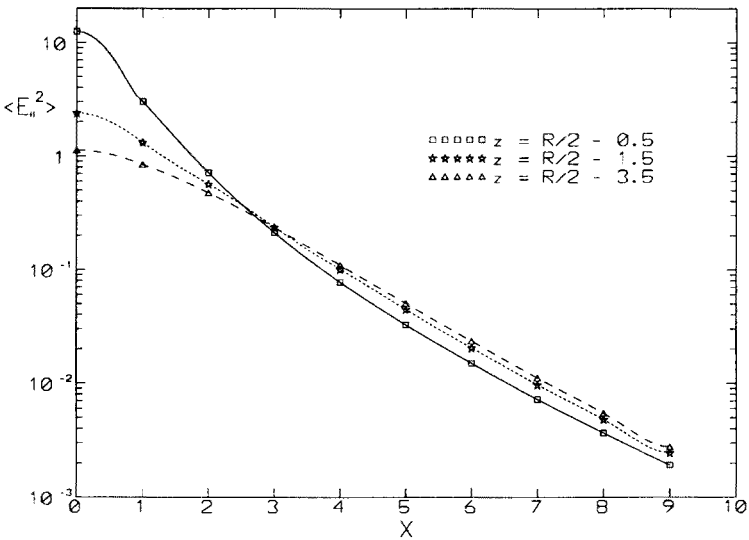

Fig. 17. Transverse dependence for $\langle E_{\|}^2 \rangle$ and various z.

Transverse dependence for the $\langle E_{\|}^2 \rangle$ is presented in Fig. 17. The solid, short-dashed and dashed lines are the profiles for $z = R/2 - 0.5$, $z = R/2 - 1.5$ and $z = R/2 - 3.5$, respectively. Again, this dependence agrees with the one shown by the classical dipole. It is monotonic, with clear maximum on the interquark axis. In addition, for every two profiles z_1, z_2 one can find such x that these curves cross (although, for instance, the classical crossing

[7] As was mentioned earlier, $\langle E_{\perp}^2 \rangle$ equals zero for the profile $z = 0$, which, in this case, is equivalent to $R/2 - 4$.

point for $z = R/2 - 0.5$ and $z = R/2 - 1.5$ takes place for $x = 1.27$ and the two lines in the figure meet at $x \approx 2.5$).

The dependence of the nonvanishing magnetic component $\langle B_\perp^2 \rangle$ on the transverse space coordinates at fixed t is generally the same as the dependence of transverse electric fields on these coordinates at fixed z because of the symmetry $z \leftrightarrow t, E \leftrightarrow B$ (exact for square loops).

Also, the counterpart of Fig. 15 can be drawn for this component showing sharp maxima for $t = \pm T/2$. This reflects the instant creation and annihilation of the charges artificially introduced by the finite Wilson loop. In continuum electrodynamics such singular effects lead to the deltas in the solutions of appropriate Maxwell equations for magnetic fields. The lattice cut-off regulates these signals so that we obtain sharp maxima.

The relations (22) obtained by many people from MC data are generally supported by the tree approximation results (excluding the interquark line which is in some sense singular and unreachable). Hence the origin of the dominance of $\langle E_\parallel^2 \rangle$ and the smallness of $\langle B_\parallel^2 \rangle$ in the MC results can be, at least partially, understood from the perturbative expansion.

5.2. Comparison with quenched results

The direct comparison of the perturbative vs. Monte Carlo data is shown in Fig. 18. The longitudinal profile for $\langle E_\parallel^2 \rangle$ for the loop $R = 6, T = 7$ is presented. Squares represent the tree approximation results. Monte Carlo data, taken from [11], are denoted by stars. We have multiplied the MC numbers by 8/3, taking into account the difference in color factors between SU(2) and SU(3), to make them comparable with the perturbative data.

This is the direct evidence for purely nonperturbative origin of the flux tube between quarks. The effect of forming the tube is in fact much stronger than one can see in this plot as all other components (which vanish in a large area between the charges in the perturbative limit) have a significant influence in the nonperturbative case. On the other hand, purely perturbative $\langle E_\parallel^2 \rangle$ is much stronger close to the charges, *i.e.* nonperturbative effects lower this value. One may say that turning on nonperturbative effects results in shifting the significant amount of energy from the vicinity of the charges to the area between them, which leads to the formation of the flux tube. This in turn, as we believe, generates confinement.

5.3. The dependence on T

In this section we will shortly discuss the dependence of the results on T. This is crucial in extracting the pure lowest state data in MC simulations and was mentioned earlier in MC sections. As an example we use $\langle E_\parallel^2 \rangle$ at the mid-point between the quarks. We examine this dependence for various R.

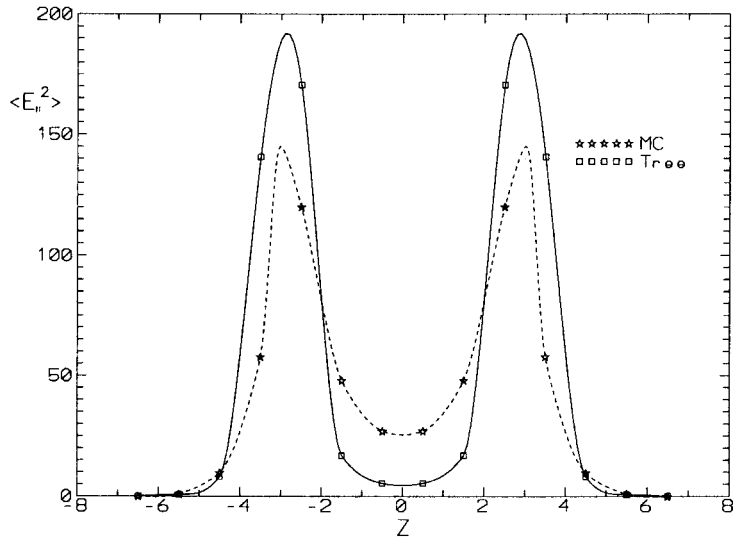

Fig. 18. Perturbative vs. Monte Carlo data: longitudinal profile for $\langle E_{\|}^2 \rangle$.

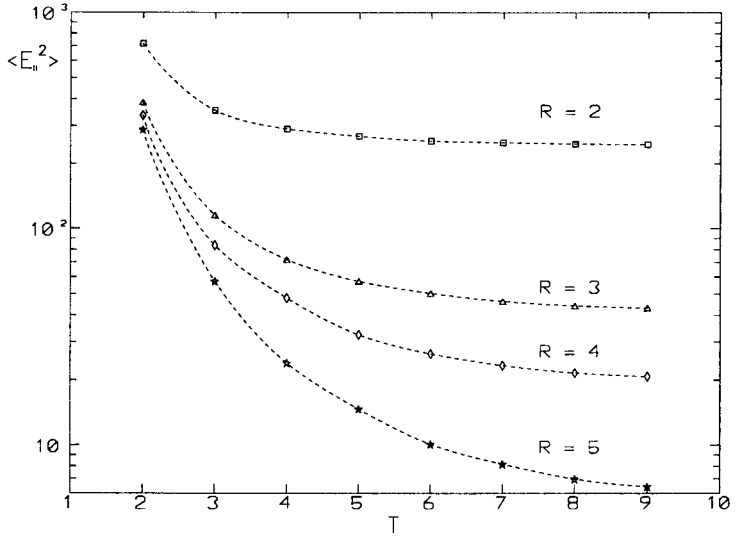

Fig. 19. $\langle E_{\|}^2 \rangle$ at the mid–point between the quarks as a function of temporal extent of the Wilson loop.

We expect that, for any fixed R, the components converge to their lowest state values when T gets large. In real measurements based on the MC data, the crucial point is how fast the components stabilize *i.e.* for which T the profiles actually describe nearly pure lowest state distribution. Also

the smoothness of the T dependence is important for reliable extrapolations [13]. We have examined this issue on our data.

Fig. 19 presents the T-dependence in the range $T = 2, \ldots, 9$ used in [11]. Note the logarithmic scale on the vertical axis. There are four sets of data points: squares, triangles, diamonds and stars for $R = 2, 3, 4, 5$, respectively. The dependence on T is quite analogous to the one obtained in [11]. The slope is clearly raising with R or, in other words, the values stabilize earlier for smaller R (at $T = 4$ for $R = 2$, $T = 7$ for $R = 3$ and $T = 9$ for $R = 4$). Only for $R = 5$ the stabilization point seems to lie beyond the scope of measured T values (compare similar effect in [11]). The resemblance of the perturbative dependence to the nonperturbative one may indicate, that the way the different energy states mix weekly depends on the coupling constant.

5.4. One loop corrections

In this section we present the results of one loop calculations performed according to the formulas derived in Section 4.3 and Appendix D. Due to the complexity of the analytic formulas and corresponding numerical expressions we limit the presentation of the results to the lattice of the size 12^4 and the Wilson loop 5×5. Since we concentrate on the differences between the tree and one loop approximation we present the data setting the coupling constant $g_0 = 1$. The scale of g_0 for which the one loop approximation can be reliable may then be approximated by comparing the appropriate tree and one loop values. We neglect the constant factor β/a^4 as well.

As in the section presenting the results of the tree approximation we start with some introductory remarks.

Generally we expect that including the one loop approximation the distribution of particular components around the quarks will no longer closely resemble the classical electric dipole. It is because this approximation involves action terms, like the Faddeev–Popov term, which have no counterparts in quantum electrodynamics.

Probably the most important difference between the tree and one loop results is the nonzero distribution of $\langle B_{\|}^2 \rangle$. This feature of the one loop approximation comes from the terms denoted $\rho^{(2)}_{22,\frac{1}{2}S_1^2,1}$ and $\rho^{(2)}_{22,S_2^W,1}$ in Appendix D (appropriate graphs are given in Figs 28 and 29). All other terms consist of direct couplings between the Wilson loop and the plaquette so that they do not contribute to the distribution of this component. However, our numerical results show that the relative contribution of $\langle B_{\|}^2 \rangle$ to the total electromagnetic field, even though nonzero, still remains the smallest.

The number of nonzero couplings (propagators) which build the one loop terms is the largest for $\langle E_{\|}^2 \rangle$ and intermediate for transverse electric and magnetic components. This is analogous to the situation we know from the tree approximation.

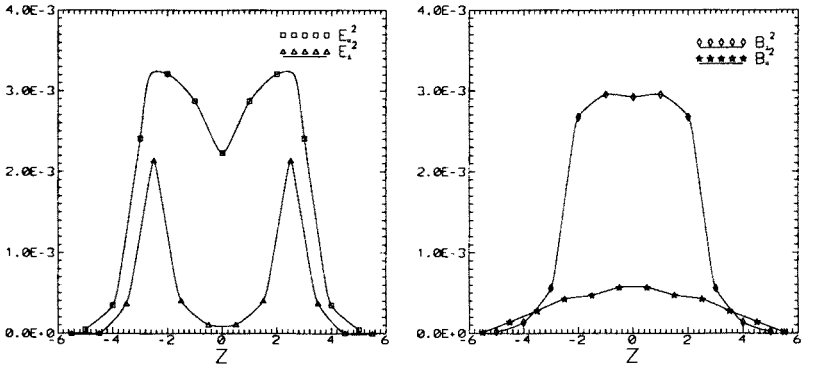

(a) (b)

Fig. 20. One loop longitudinal profiles for electric and magnetic components.

Below we show the one loop results obtained by numerical evaluation of the formulas derived in section 4.3. We *do not* combine them with the tree results.

Fig. 20 presents the longitudinal profiles for the electric and magnetic components. Both electric profiles have the maxima near the quark locations, like in the tree approximation. The values which they take at their maximum values are comparable although $\langle E_{\|}^2 \rangle$ is generally much larger along the profile. The profile for the magnetic longitudinal component is qualitatively different from the electric profiles taking the maximal value at the center of the loop (*i.e.* at the mid-point between the quarks). Also the other magnetic component is concentrated between the quarks. However, this behaviour may be, at least partially, connected with the small size of the Wilson loop and the lattice. Note also, that we are not exactly on the interquark line (it was explained in the MC section). As we stated above the contribution of $\langle B_{\|}^2 \rangle$ to the total chromoelectromagnetic field is still the smallest but the sign of this contribution is in agreement with the MC results for $\langle B_{\|}^2 \rangle$ (note that the tree distribution for this components was zero in the whole space-time so that we use the one loop results for comparisons with the MC data).

Fig. 21 presents the comparison between the one loop contributions of all components along the transverse direction (starting, as usual, from the

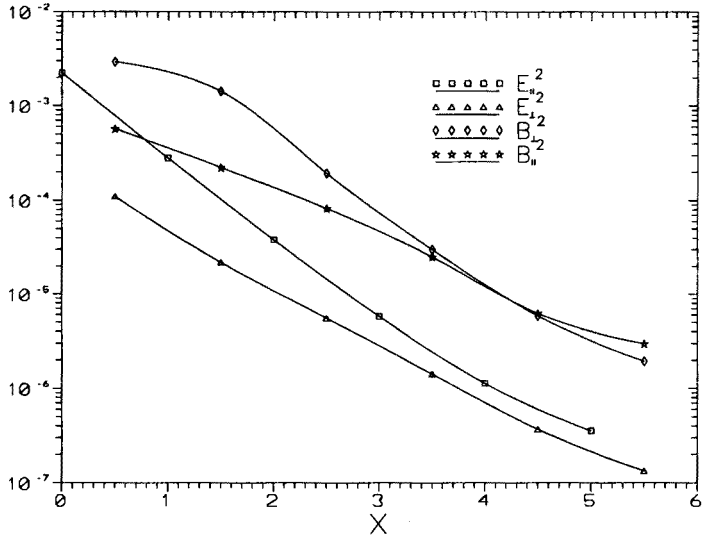

Fig. 21. One loop transverse profiles at $z = 0$.

mid-point between the quarks). As expected intuitively all of them are decreasing functions of the distance from the Wilson loop.

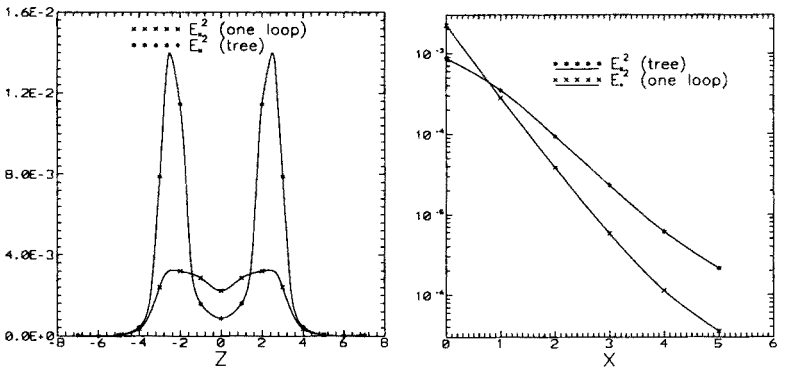

(a) (b)

Fig. 22. One loop vs. tree approximation — longitudinal and transverse dependence for $\langle E_{\parallel}^2 \rangle$.

Fig. 22 compares the tree and one loop contributions for $\langle E_{\parallel}^2 \rangle$ at $g_0 = 1$. As expected, in the perturbative region near the sources the tree contribution dominates more over the higher order one than in the nonperturbative region between the quarks and outside the dipole. The superposition of the

two contributions can lead to the flattening of the profile observed in nonperturbative results (*cf.* Fig. 18). Along the transverse profile we observe the monotonic fall off of both contributions with the one loop contribution decreasing significantly faster.

5.5. Summary of analytic results

The most important results of the perturbative section which we would like to stress are:

1. The distribution of the color fields around the quark dipole in the tree approximation closely resembles the distribution of the electromagnetic field around the classical dipole. It is in agreement with our expectations based on the direct correspondence between lowest order action terms in QED and QCD.
2. The color field in the tree approximation (reduced in this case to the electric longitudinal component) has sharp maxima in the vicinity of the charges and decreases rapidly toward a zero value in the region between the quarks. This behavior is in contrast with the MC results where we observe the formation of the flux tube and the field decreases slower when we enter the interquark area.
3. The dependence of $\langle E_{\|}^2 \rangle$ on T, which turned out to be similar to the distribution obtained from the MC measurements, suggests that the way the different quantum states contribute to the total field may weekly depend on the coupling constant.
4. The one loop results slighty correct the picture obtained in the tree approximation. The superposition of these two contributions has more in common with the MC results. The nonzero distribution of $\langle B_{\|}^2 \rangle$ is the most important result of including the one loop approximation.
5. The relative strength of the tree and one loop contributions identifies perturbative and nonperturbative regions around the sources.

6. Conclusions and summary

We carried out rather extensive study of the distribution of the chromoelectric and chromomagnetic field around the static quark–antiquark pair. The study was performed using both Monte Carlo (nonperturbative) and analytic (perturbative) approaches.

The Monte Carlo results have been obtained from the configurations with dynamical fermions, at $\beta = 5.35$. They are the first nonquenched data obtained for considerably large lattices ($16^3 \times 24$). Although these results are generally in agreement with the quenched ones published earlier by many authors, we have also found some interesting differences, among them the

effect of breaking the flux tube and the differences in the distribution of the energy and action density. We also stressed the need of including the quark condensate to completely describe the $q\bar{q}$ system. It is also apparent that we need much better statistics to reduce significantly the errors for greater Wilson loops. Examining larger interquark separations seems to be crucial for understanding the mechanism of breaking the flux tube and the origin of confinement. Finally, an alternative method of computing the field distribution was checked against the standard one. Having an advantage of automatically approximating the results for large T this method may be successfully used in future, more precise studies.

The analytic calculations have been performed mainly to see which details of the color field distribution obtained using Monte Carlo methods are purely nonperturbative and which can be understood basing on the perturbative expansion of the QCD action (*i.e.* using weak coupling approximation). As we expected, the formation of the flux tube, responsible for confinement, is an example of such nonperturbative effects which cannot be derived perturbatively. On the other hand, rather surprisingly, the dependence of the longitudinal electric component on T is similar in the Monte Carlo and in the perturbative approach. It implies that the way the different quantum states mix in the total field (which directly influences the T dependence) may be independent of the coupling constant. Finally, we proved the nonzero distribution of the longitudinal chromomagnetic component in the one loop approximation and we found that the one loop corrections are consistent with our expectations based on the tree order and MC results.

I wish to express my gratitude to Jacek Wosiek who proposed me that very interesting subject and patiently acquainted me with the lattice methods. I deeply appreciate his guidance and remarks. Also I would like to thank R. Wit who acquainted me with modern numerical methods. Finally, I thank E. Laermann and F. Karsch for their support and hospitality during my work at HLRZ Jülich.

Appendix A

Fast Fourier Transform in MC and in perturbative calculations

As mentioned in Sections 2.4, 4.2 and 4.3 special numerical methods based on the Fast Fourier Transform (FFT) were used both in Monte Carlo and weak coupling computations presented in this work.

The FFT — a fast algorithm for numerical evaluating of the discrete Fourier Transform [44] became generally known in the 60s, although it was developed and used much earlier. In the standard formulation it can be

applied to the data sets consisting of $N_V = 2^k$ real or complex numbers, accelerating the computations by a factor of $N_V/\log_2 N_V$ comparing to the ordinary method of computing FT. For the data vector composed of all $N_V = 16^3 \times 24$ sites of the lattice used in this work this factor is rougly 6000.

Crucial for the use of the FFT in the Monte Carlo computations performed in this work is the *discrete correlation theorem* [44]. It relates the correlation of two discrete real functions, each periodic with period N_V, to their Fourier Transforms

$$\mathrm{FT}\left(\mathrm{Corr}(g,h)\right) = \mathrm{FT}(g)\mathrm{FT}(h)^{\star}, \tag{85}$$

where the correlation is defined as

$$\mathrm{Corr}(g,h)_j = \sum_{k=0}^{N_V-1} g_{j+k}h_k\,, \tag{86}$$

and the Fourier Transform

$$FT(h)_s = \sum_k \mathrm{e}^{iks}h_k\,. \tag{87}$$

For given MC configuration, fixed orientation of the Wilson loop in the subspace xyz and particular component of the color field there are N_V possible pairs (Wilson loop, plaquette) representing the same physical space-time point (translational symmetry, Section 2.4). Grouping all Wilson loops in 1-dimensional vector g and all plaquettes — in vector h we can apply the above theorem directly, computing at once all required correlations (*i.e.* field strength for all physical space-time points) averaged over the translational symmetry.

Using FFT requires the length of the input vectors to be a power of two. It can be accomplished by extending their length, duplicating the data in one of them and zero-padding remaining free slots in both[8]. Although the resulting vectors are much longer the problem can be still efficiently solved using vectorized FFT subroutines from the CRAY math library.

The FFT was also extensively used in the weak coupling section of this work. All calculations have been finally performed in configuration space and the results expressed in terms of free gluonic propagators

$$D_{\mu\nu}(0,x) = \frac{\delta_{\mu\nu}}{N_V}\sum_p \frac{\mathrm{e}^{ipx}}{8 - 2\sum_{\lambda=1}^{4}\cos p_\lambda}\,, \tag{88}$$

[8] Simple extension to the next nearest power of two and zero-padding changes the value of the correlation

where p takes discrete values: $p_\lambda = 2\pi k_\lambda / N_\lambda$, $k_\lambda = 0, 1, \ldots, N_\lambda - 1$ and $N_V = N_1 N_2 N_3 N_4$ is the total number of lattice sites.

This formula is the (inverse) 4-dimensional FT of the momentum propagator, and can be effectively evaluated using FFT. We implemented the 4–dimensional algorithm working well for any set of N_λs (not only powers of two). Using it, one can compute the propagators once for particular lattice and then store them on disk and reuse for various Wilson loops and field components. Appropriate disk file can be effectively compressed using the symmetry implied by periodic boundary conditions, so that the time needed for reading it can be neglected compared to that of the actual computations. The same technique has been also applied to the Faddeev–Popov ghost weights (Appendix D, Eq. (136)).

Appendix B

Wilson loop up to g^4

Using the definitions of the Wilson loop (4) and the link variable U_l (1) one can compute the coefficients w_i in the series (52). The simplest way to do it is to use the Baker–Hausdorff formula

$$exp(X)\exp(Y) = \exp\left(X + Y + \tfrac{1}{2}[X,Y] + \tfrac{1}{12}[X,[X,Y]] + \tfrac{1}{12}[[X,Y],Y] + \ldots\right) \quad (89)$$

extended to the case of many exponents. Taking advantage of the well known properties of the trace and SU(3) generators (the commutator and the A are traceless, $\mathrm{Tr}AB = \mathrm{Tr}BA$) we obtain for particular w_is (for convenience we introduced auxilliary subterms for w_3 and w_4: $w_i = \sum_k w_{i,k}$)

$$w_2 = \frac{1}{2n}\mathrm{Tr}\left(\sum_l A_l\right)^2, \quad (90)$$

$$w_{3,1} = \frac{1}{6n}\mathrm{Tr}\left(\sum_l A_l\right)^3, \quad (91)$$

$$w_{3,2} = \frac{1}{2n}\mathrm{Tr}\left(\sum_{l,m<n} A_l[A_m, A_n]\right), \quad (92)$$

$$w_{4,1} = \frac{1}{4n}\mathrm{Tr}\left(\left(\sum_l A_l\right)^2 \sum_{m<n}[A_m, A_n]\right), \quad (93)$$

$$w_{4,2} = \frac{1}{8n}\mathrm{Tr}\left(\sum_{l<m}[A_l, A_m]\right)^2, \tag{94}$$

$$w_{4,3} = \frac{1}{4n}\mathrm{Tr}\left(\sum_l A_l \sum_{m<n<p}[[A_m, A_n], A_p]\right), \tag{95}$$

$$w_{4,4} = \frac{1}{12n}\mathrm{Tr}\left(\sum_l A_l \sum_{(m,n)<p}[A_m, [A_n, A_p]]\right), \tag{96}$$

$$w_{4,5} = \frac{1}{12n}\mathrm{Tr}\left(\sum_l A_l \sum_{m<n}[[A_m, A_n], A_n]\right), \tag{97}$$

$$w_{4,6} = \frac{1}{24n}\mathrm{Tr}\left(\sum_l A_l\right)^4, \tag{98}$$

where A_l is the gauge field coupled to the link l. The sums are defined as oriented, *i.e.* the notation $l < m$ means, that the link l comes before the link m on the oriented loop. The gauge fields should be preceded by the minus sign if taken from the second half of the loop, so that for the plaquette the sum $\sum_l A_l$ represents $F_{\mu\nu}$.

Appendix C

The action terms

In this appendix we list all contributions to the action needed for perturbative calculations up to one loop order [41, 45–50]. The notation was introduced in Section 4.1. For convenience we have choosen the sign in the exponent of the Feynman amplitude to be positive *i.e.* e^S instead of e^{-S}, where S is the weak coupling action. Also, the coupling constant is defined as ig_0 . These conventions influence the signs in the formulas presented below.

The structure constants f^{abc} and the coefficients d^{abc} are defined as follows

$$\{T^a, T^b\} = \tfrac{1}{3}\delta^{ab} + d^{abc}T^c \ \text{(symmetric)}, \tag{99}$$

$$[T^a, T^b] = if^{abc}T^c \ \text{(antisymmetric)}. \tag{100}$$

S_0 denotes the zeroth order term in the Wilson action plus the gauge fixing term (in Feynman gauge). These terms yield the free propagator $\langle AA\rangle_0$

$$S_0 = -\tfrac{1}{4}\sum_{x\mu\nu} F^a_{\mu\nu}(x)F^a_{\mu\nu}(x) - \tfrac{1}{2}\sum_{x\mu\nu}\Delta_\mu A^a_\mu(x)\Delta_\nu A^a_\nu(x), \tag{101}$$

where $F_{\mu\nu}(x) = \Delta_\mu A_\nu(x) - \Delta_\nu A_\mu(x)$ and $\Delta_\mu A_\nu(x) = A_\nu(x+\mu) - A_\nu(x)$.

S_1 is the first order term of the expansion of the Wilson action

$$S_1 = -\frac{i}{4n} f^{abc} \sum_{x\mu\nu} F^a_{\mu\nu}(x) \left(A^b_\mu(x) A^c_\nu(x) + A^b_\mu(x+\nu) A^c_\nu(x+\mu) \right). \quad (102)$$

S_2^W is the second order term

$$S_2^W = \frac{1}{n} \sum_{x\mu\nu} \Big\{ f^{cab} f^{cde} \left(\tfrac{1}{16} \Pi^{abde}_{\mu\nu,1}(x) - \tfrac{1}{48} \Pi^{abde}_{\mu\nu,2}(x) - \tfrac{1}{24} \Pi^{abde}_{\mu\nu,3}(x) + \tfrac{1}{192} \Pi^{abde}_{\mu\nu,4}(x) \right)$$
$$- \left(\tfrac{1}{2} d^{cab} d^{cde} + \tfrac{1}{3} \delta^{ab} \delta^{de} \right) \tfrac{1}{96} \Pi^{abde}_{\mu\nu,4}(x) \Big\}, \quad (103)$$

where

$$\Pi_1^{abde} = \left(A^a_\mu(x) A^b_\nu(x) + A^a_\mu(x+\nu) A^b_\nu(x+\mu) \right) \times \left(A^d_\mu(x) A^e_\nu(x) + A^d_\mu(x+\nu) A^e_\nu(x+\mu) \right), \quad (104)$$

$$\Pi_2^{abde} = \left(A^a_\mu(x) - A^a_\nu(x) \right) F^b_{\mu\nu}(x) \left(A^d_\mu(x) - A^d_\nu(x) \right) F^e_{\mu\nu}(x), \quad (105)$$

$$\Pi_3^{abde} = F^a_{\mu\nu}(x) \Big\{ \left(A^b_\mu(x) + A^b_\nu(x) \right) A^d_\mu(x) A^e_\nu(x) - \left(A^b_\mu(x+\nu) + A^b_\nu(x+\mu) \right) A^d_\mu(x+\nu) A^e_\nu(x+\mu) \Big\}, \quad (106)$$

and

$$\Pi_4^{abde} = F^a_{\mu\nu} F^b_{\mu\nu} F^d_{\mu\nu} F^e_{\mu\nu}. \quad (107)$$

The above terms can be directly derived from the expansion of the Wilson loop restricted to the case of the plaquette. The antisymmetry of the group structure constants f^{abc} and the properties of the trace mentioned in Appendix B considerably simplify this derivation. All required input formulas are given in Appendix B.

The remaining S_2 terms are the measure term

$$S_2^M = \frac{n}{24} \sum_{x\mu} A^a_\mu(x) A^a_\mu(x) \quad (108)$$

and the Faddeev–Popov term

$$S_2^{\mathrm{FP}} = \frac{n}{48} \sum_{x\mu} A^a_\mu(x) A^a_\mu(x) - \frac{n}{2N_V^2} \sum_{\substack{pk \\ \mu\nu}} \frac{\hat{k}_\mu \left(1 + \frac{1}{2} \hat{p}^\star_\mu \right) \hat{p}_\nu \left(1 + \frac{1}{2} \hat{k}^\star_\nu \right)}{(\hat{k}\hat{k}^\star)(\hat{p}\hat{p}^\star)} A^a_\mu(k-p) A^a_\nu(p-k), \quad (109)$$

where $\hat{k}_\mu = e^{-ik_\mu} - 1$ and N_V is the volume of the lattice.

Appendix D

$\langle WP \rangle$ terms

In this appendix we write down computer-ready expressions analogous to (76), for one loop terms listed in Section 4.3, equations (80)–(84). They are based on formulas given in Appendices B and C. The letters $k, l, \ldots$ and $k', l', \ldots$ denote links along the Wilson loop and the plaquette, respectively. The gauge field A may be written in two forms: A_l is connected with the link l on the Wilson loop (plaquette) and $A_\mu(x)$ — with the site x of the Euclidean space. These two notations are equivalent: $A_l = A_{\mu(l)}(x(l))$. The meaning of the constraints like $l < m$ was explained in Appendix B. The loops in the graphs represent the Wilson loop (on the left) and the plaquette. The lines represent the propagators.

The term (80) illustrated by graph in Fig. 23 is

$$w_2^{(0)} = \frac{n^2 - 1}{4n} \sum_{lm} D_{lm}. \tag{110}$$

The next one, $\rho_{22}^{(0)}$ (Fig. 24) was already written down as (76). Two mutually symmetric terms, $\rho_{24}^{(0)}$ and $\rho_{42}^{(0)}$ correspond to graph type presented in Fig. 25. We will discuss the latter. According to formulas given in Appendix B there are 6 subterms $w_{4,1} \ldots w_{4,6}$ of w_4

$$\langle w_4 p_2 \rangle_0^c = \langle w_{4,1} p_2 \rangle_0^c + \ldots + \langle w_{4,6} p_2 \rangle_0^c. \tag{111}$$

Now one can separate the color part and write

$$\langle w_{4,1} p_2 \rangle_0^c = \frac{i}{64n^2} (d^{abe} f^{cde} + i f^{abe} f^{cde}) \times \sum_{kl} \sum_{m<n} \sum_{r's'} \langle A_k^a A_l^b A_m^c A_n^d A_{r'}^{a'} A_{s'}^{a'} \rangle_0. \tag{112}$$

Using the Wick theorem the above formula can be expanded according to graph in Fig. 25, giving 12 products [9] of three propagators: $D_{kl} D_{mr'} D_{ns'}$, $\ldots$, $D_{mn} D_{ks'} D_{lr'}$. Supressing the color indices (thanks to deltas introduced by the propagators) and using the symmetries in color and link indices we find that 4 of these products are preceded by the color coefficient including

[9] Of the 15 products possible here 3 vanish since we use connected correlations.

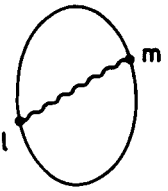

Fig. 23.

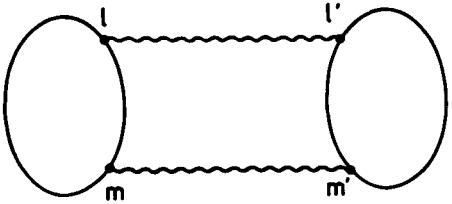

Fig. 24.

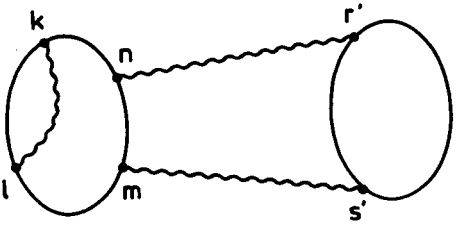

Fig. 25.

f^{aab}, which equals zero, and among remaining 8 products there are 4 pairs of mutually compensating terms. Finally

$$\langle w_{4,1}p_2\rangle_0^c = 0. \tag{113}$$

Quite analogous considerations lead to following results for remaining terms of $\rho_{42}^{(0)}$

$$\langle w_{4,2}p_2\rangle_0^c = \frac{C_f}{32n^2}\sum_{l<m}\sum_{n<k}\sum_{s'r'}(2D_{lk}D_{ms'}D_{nr'} - D_{ln}D_{ms'}D_{kr'} - D_{mk}D_{ls'}D_{nr'}), \tag{114}$$

where $C_f = f^{abc}f^{abc}$,

$$\langle w_{4,3}p_2\rangle_0^c = \frac{C_f}{16n^2}\sum_{k}\sum_{l<m<n}\sum_{r's'}(D_{kl}D_{mr'}D_{ns'} - D_{km}D_{lr'}D_{ns'} - D_{ln}D_{kr'}D_{ms'} + D_{mn}D_{kr'}D_{ls'}), \tag{115}$$

$$\langle w_{4,4}p_2\rangle_0^c = 0, \tag{116}$$

$$\langle w_{4,5}p_2\rangle_0^c = \frac{C_f}{48n^2}\sum_k\sum_{l<m}\sum_{r's'}(D_{kl}D_{mr'}D_{ms'} - D_{km}D_{lr'}D_{ms'} - D_{lm}D_{kr'}D_{ms'} + D_{mm}D_{kr'}D_{ls'}), \tag{117}$$

$$\langle w_{4,6}p_2\rangle_0^c = \frac{1}{24n^2}\left\{\frac{(n^2-1)^2}{12} + \frac{n^2-1}{6} + \frac{1}{8}C_{d1} + \frac{1}{4}C_{d2}\right\} \times \sum_{k\ldots s'} D_{kl}D_{mr'}D_{ns'}, \tag{118}$$

where $C_{d1} = d^{aac}d^{cbb}$ and $C_{d2} = d^{abc}d^{abc}$.

Next we will analyse the subterms of $\rho_{33}^{(0)} = \langle w_3p_3\rangle_0$. Appropriate graphs are shown in Fig. 26. Using the formulas (91) and (92) and evaluating the trace we can write for w_3

$$w_3 = \frac{1}{24n}d^{abc}\sum_{lmn}A_l^aA_m^bA_n^c + \frac{1}{24n}if^{abc}\sum_{lmn}A_l^aA_m^bA_n^c + \frac{1}{4n}\mathrm{i}f^{abc}\sum_{l,m<n}A_l^aA_m^bA_n^c. \tag{119}$$

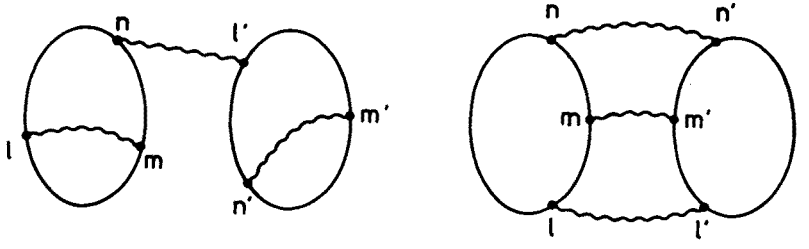

Fig. 26.

Using the same formula for p_3 and taking into account the symmetries in color and link indices we find that only two of nine products possible here are nonzero giving the final form

$$\langle w_3p_3\rangle_0 = \frac{1}{64n^2}C_{d1}\sum_{\substack{lmn\\l'm'n'}}D_{lm}D_{nl'}D_{m'n'}$$

$$+\frac{1}{96n^2}C_{d2}\sum_{\substack{lmn\\l'm'n'}} D_{ll'}D_{mm'}D_{nn'}$$

$$-\frac{1}{16n^2}C_f\sum_{\substack{l,m<n\\l',m'<n'}}\{\,D_{ll'}(D_{mm'}D_{nn'}-D_{mn'}D_{nm'})$$

$$+D_{lm'}(D_{mn'}D_{nl'}-D_{ml'}D_{nn'})$$

$$+D_{ln'}(D_{ml'}D_{nm'}-D_{mm'}D_{nl'})\,\}\,. \tag{120}$$

Now we turn to the terms involving action parts listed in Appendix C. The term (83) will be analyzed first. Appropriate graph is presented in Fig. 27. Combining the formulas (90), (119) and (102), after some cancellations due to color symmetries, we obtain

$$\rho_{23}^{(1)}=\frac{C_f}{32n^3}\sum_{lm}\sum_{\substack{l'\\m'<n'}}\sum_{x\mu\nu}\sum_{''4''}\left(\underbrace{D_{ll'}D_{mx_\alpha}D_{m'x_\beta}D_{n'x_\gamma}\pm\cdots}_{18\text{ products}}\right). \tag{121}$$

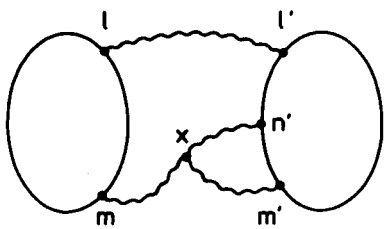

Fig. 27.

The sum denoted by $\sum_{''4''}$ deals with the indices x_α, x_β , x_γ and means the summation over four different products yielded by (102). The (*site*, *direction*) pairs which they represent for all four components of this sum are as follows:

	term	*I*	*II*	*III*	*IV*
x_α	$\leftrightarrow$	$(x+\mu,\nu)$	$(x+\mu,\nu)$	(x,μ)	(x,μ)
x_β	$\leftrightarrow$	(x,μ)	$(x+\nu,\mu)$	(x,μ)	$(x+\nu,\mu)$
x_γ	$\leftrightarrow$	(x,ν)	$(x+\mu,\nu)$	(x,ν)	$(x+\mu,\nu)$.

The four-propagator products are generated according to the Wick theorem and correspond to the graph 27. Half of them are preceded by the minus sign due to antisymmetry of f^{abc}. This formula, although rather complicated, can be substantially optimized at a run-time.

Remaining terms in the expansion of $\langle WP \rangle$ involve parts connected with $\tilde{S}_2$ denoted collectively by $\rho_{22}^{(2)}$ in Section 4.3. Two graphs in Fig. 28 represent terms originating from $\frac{1}{2}S_1^2$. The general formula for this types of graphs can be obtained using (90) and (102).

$$\frac{1}{2}w_2 p_2 S_1^2 = -\frac{1}{128n^4} f^{abc} f^{a'b'c'} \sum_{\substack{lm \\ l'm'}} \sum_{\substack{x\mu\nu \\ y\sigma\tau}} \sum_{\text{"16"}} A_l^d A_m^d A_{l'}^{d'} A_{m'}^{d'} A_{x_\alpha}^a A_{x_\beta}^b A_{x_\gamma}^c A_{y_\delta}^{a'} A_{y_\varepsilon}^{b'} A_{y_\zeta}^{c'}, \tag{122}$$

where $x_\alpha, x_\beta, x_\gamma$ can be $(x+\mu,\nu),\ldots,(x,\mu)$ and $y_\delta, y_\varepsilon, y_\zeta$ - $(y+\sigma,\tau),\ldots,(y,\sigma)$ according to the same convention concerning $\sum_{\text{"16"}}$ as in (121).

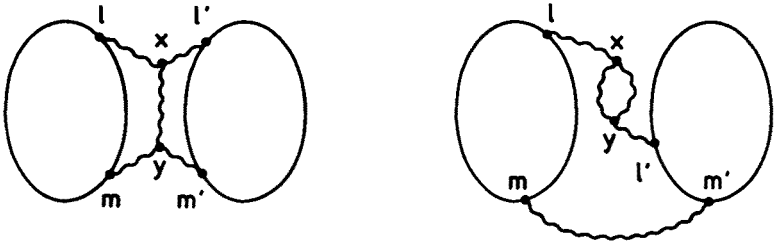

Fig. 28.

In particular, the graphs in Fig. 28 are

$$\rho^{(2)}_{22,\frac{1}{2}S_1^2,1} = -\frac{C_f}{128n^4} \sum_{\substack{lm \\ l'm'}} \sum_{\substack{x\mu\nu \\ y\sigma\tau}} \sum_{\text{"16"}} \left(\underbrace{D_{lx_\alpha} D_{my_\delta} D_{l'x_\beta} D_{m'y_\varepsilon} D_{x_\gamma y_\zeta} \pm \cdots}_{\text{36 products}} \right) \tag{123}$$

and

$$\rho^{(2)}_{22,\frac{1}{2}S_1^2,2} = -\frac{C_f}{128n^4} \sum_{\substack{lm \\ l'm'}} \sum_{\substack{x\mu\nu \\ y\sigma\tau}} \sum_{\text{"16"}} \left(\underbrace{D_{lx_\alpha} D_{l'y_\delta} D_{x_\beta y_\varepsilon} D_{x_\gamma y_\zeta} D_{mm'} \pm \cdots}_{\text{18 products}} \right), \tag{124}$$

respectively.

Graphs introduced by the second order term of the Wilson action, S_2^W, are presented in Fig. 29. Appropriate terms can be obtained from (90) and (103). All these terms have the part $A_{x_\alpha} A_{x_\beta} A_{x_\gamma} A_{x_\delta}$ in common. The composite indices $x_\alpha, \ldots, x_\delta$ represent the various combinations of the

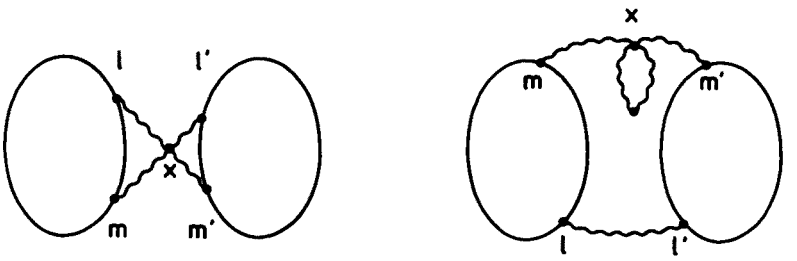

Fig. 29.

(*site*, *direction*) pairs corresponding to the S_2^W terms listed in Appendix C. This notation is analogous to the one introduced in (121). Combining this four-field part with the expressions for w_2 and p_2 yields the generic form of the terms forming $\rho^{(2)}_{22,S_2^W}$

$$Y^{abde} A^s_l A^s_m A^{s'}_{l'} A^{s'}_{m'} A^a_{x_\alpha} A^b_{x_\beta} A^d_{x_\gamma} A^e_{x_\delta}, \tag{125}$$

where Y^{abde} can be $f^{cab}f^{cde}$ or $d^{cab}d^{cde}$ or $\delta^{ab}\delta^{de}$ according to (103).

Evaluation of this term using the Wick theorem produces following results. For the graph on the left, term $\rho^{(2)}_{22,S_2^W,1}$, we have 16 nonzero products of the type

$$C_f D_{lx_\alpha} D_{mx_\beta} D_{l'x_\gamma} D_{m'x_\delta}, \tag{126}$$

(half of them are preceded by the minus sign), 8 products of type

$$C_{d1} D_{lx_\alpha} D_{mx_\beta} D_{l'x_\gamma} D_{m'x_\delta}, \tag{127}$$

16 products of the type

$$C_{d2} D_{lx_\alpha} D_{mx_\beta} D_{l'x_\gamma} D_{m'x_\delta}, \tag{128}$$

and 24 products of the type

$$D_{lx_\alpha} D_{mx_\beta} D_{l'x_\gamma} D_{m'x_\delta}, \tag{129}$$

(for clarity, all constant multipliers have been neglected).

Appropriate counts for the second graph, term $\rho^{(2)}_{22,S_2^W,2}$, are: 32 products of the type

$$C_f D_{ll'} D_{mx_\alpha} D_{m'x_\gamma} D_{x_\beta x_\delta}, \tag{130}$$

16 products of the type

$$C_{d1} D_{ll'} D_{mx_\alpha} D_{m'x_\gamma} D_{x_\beta x_\delta}, \tag{131}$$

32 products of the type

$$C_{d2}D_{ll'}D_{mx_\alpha}D_{m'x_\gamma}D_{x_\beta x_\delta}, \tag{132}$$

and 48 products of the type

$$D_{ll'}D_{mx_\alpha}D_{m'x_\gamma}D_{x_\beta x_\delta}. \tag{133}$$

The measure term, S_2^M, (Fig. 30) can be derived from (90) and (108):

$$\rho^{(2)}_{22,S_2^M} = \frac{n^2-1}{48n}\sum_{x\mu}\sum_{\substack{lm\\ l'm'}} D_{l,x\mu}D_{l',x\mu}D_{mm'}. \tag{134}$$

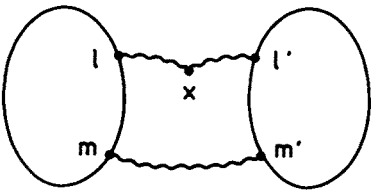

Fig. 30.

Faddeev–Popov action consists of two main parts. The former, local, has the same structure as the measure term so that it can be included into the formula (134) changing the overall factor. The latter needs some additional evaluation to fit into our computational scheme. Turning to configuration space we obtain for this part

$$S^{\mathrm{FP}}_{2,2} = -\tfrac{1}{2}n\sum_{\substack{xy\\ \mu\nu}} A^a_\mu(x)A^a_\nu(y)R_{\mu\nu}(y-x)R_{\nu\mu}(x-y), \tag{135}$$

where

$$R_{\mu\nu}(u) = \sum_k \frac{\hat{k}_\mu\left(1+\frac{1}{2}\hat{k}^\star_\nu\right)}{\hat{k}\hat{k}^\star}\mathrm{e}^{-\mathrm{i}ku}. \tag{136}$$

Hence

$$\rho^{(2)}_{22,S^{\mathrm{FP}}_{2,2}} = -\frac{n^2-1}{4n}\sum_{\substack{xy\\ \mu\nu}}\sum_{\substack{lm\\ l'm'}} R_{\mu\nu}(y-x)R_{\nu\mu}(x-y)D_{ll'}D_{m,x\mu}D_{m',y\nu}. \tag{137}$$

The coefficients R can be computed using FFT (Appendix A).

REFERENCES

[1] J. Kogut, *Phys. Rev.* **D12**, 3501 (1974).
[2] A. Chodos, R.L. Jaffe, K. Johnson, V.F. Weisskopf, *Phys. Rev.* **D9**, 3471 (1974).
[3] C.N. Yang, R.L. Mills, *Phys. Rev.* **96**, 191 (1954).
[4] M. Creutz, *Quarks, Gluons and Lattices,* Cambridge University Press 1983.
[5] K.G. Wilson, *Phys. Rev.* **D10**, 2445 (1974).
[6] J.B. Kogut, *Rev. Mod. Phys.* **51**, 659 (1979).
[7] J.B. Kogut, *Rev. Mod. Phys.* **55**, 775 (1983).
[8] M. Fukugita, T. Niuya, *Phys. Lett.* **132B**, 374 (1983).
[9] J. Flower, S. Otto, *Phys. Lett.* **160B**, 128 (1985).
[10] J. Wosiek, R.W. Haymaker, *Phys. Rev. Rapid Comm.* **D36**, 3297 (1987).
[11] R.W. Haymaker, J. Wosiek, *Acta Phys. Pol.* **B21**, 403 (1990).
[12] R.W. Haymaker, J. Wosiek, *Phys. Rev.* **D43**, 2676 (1991).
[13] R.W. Haymaker, V. Singh, J. Wosiek, LSU HE Preprint No. 94-159.
[14] C. Michael, *Nucl. Phys.* **B280**, 13 (1987).
[15] R. Sommer, *Nucl. Phys.* **B291**, 673 (1987).
[16] R. Sommer, *Nucl. Phys.* **B306**, 180 (1988).
[17] I.H. Jorysz, C. Michael, *Nucl. Phys.* **B302**, 448 (1987).
[18] G.S. Bali, K. Schilling, CERN–TH.7413/94.
[19] H. Hamber, G. Parisi, *Phys. Rev. Lett.* **47**, 1792 (1981).
[20] D. Weingarten, *Phys. Lett.* **109B**, 57 (1982).
[21] E. Marinari, G. Parisi, C. Rebbi, *Phys. Rev. Lett.* **47**, 1795 (1981).
[22] W. Feilmair, H. Markum, *Nucl. Phys.* **B370**, 299 (1992).
[23] E. Laermann, P. Schildberg, *Nucl. Phys.* **B30**, (Proc. Suppl.)., 503 (1993).
[24] T. Barczyk, R.W. Haymaker, V. Singh, E. Laermann, J. Wosiek, *Nucl. Phys.* **B26** (Proc. Suppl.)., 462 (1992).
[25] T. Barczyk, *Nucl. Phys.* **B30** (Proc. Suppl.)., 499 (1993).
[26] R. Gupta, C.F. Baillie, R.G. Brickner, G.W. Kilcup, A. Patel, S.R. Sharpe, *Phys. Rev.* **D44**, 3272 (1991).
[27] G. Parisi, *Statistical Field Theory,* Addison–Wesley Publishing Company, Inc. 1988.
[28] K. Binder, D.W. Hermann, *Monte Carlo Simulation in Statistical Physics,* Springer-Verlag, 1988.
[29] N. Metropolis, A. Rosenbluth, M. Rosenbluth, A. Teller, E. Teller, *J. Chem. Phys.* **21**, 1087 (1953).
[30] M. Fukujita, Y. Oyanagi, A. Ukawa, *Phys. Rev.* **D36**, 824 (1987).
[31] J.R. Westlake, *A Handbook of Numerical Matrix Inversion and Solution of Linear Equations,* Wiley 1965.
[32] T. Barczyk, R. Wit, *Acta Phys. Pol.* **B22**, 623 (1991).
[33] R. Ben-Av, A. Brandt, M. Harmatz, E. Katznelson, P.G. Lauwers, S. Solomon, K. Wolowesky, Fermion Simulations Using Parallel Transported Multigrid, Bonn University preprint BONN-HE-90-11.
[34] R. Ben-Av, A. Brandt, S. Solomon, *Nucl. Phys.* **B329**, 193 (1990).

[35] J. Wosiek, *Acta Phys. Pol.* **B18**, 519 (1987).
[36] S. Duane, A.D. Kennedy, B.J. Pendleton, D. Roweth, *Phys. Lett.* **B195**, 216 (1987).
[37] S. Gottlieb, W. Liu, D. Toussaint, R.L. Renken, R.L. Sugar, *Phys. Rev.* **D35**, 2531 (1987).
[38] S. Duane, J. Kogut, *Phys. Rev. Lett.* **55**, 2774 (1985).
[39] A. Ukawa, M. Fukugita, *Phys. Rev. Lett.* **55**, 1854 (1985).
[40] L.D. Faddeev, V.N. Popov, *Phys. Lett.* **25B**, 29 (1967).
[41] B.E. Baaquie, *Phys. Rev.* **D16**, 2612 (1977).
[42] T. Barczyk, *Acta Phys. Pol.* **B24**, 1131 (1993).
[43] B.W. Kernighan, D.M. Ritchie, The C Programming Language, Englewood Cliffs, NJ: Prentice Hall, 1988.
[44] W.H. Press, S.A. Teukolsky, W.T. Vetterling, B.P. Flannery, *Numerical Recipes in C*, Cambridge University Press, 1992.
[45] A. Hasenfratz, P. Hasenfratz, *Phys. Lett.* **93B**, 165 (1980).
[46] A. Di Giacomo, G.C. Rossi, *Phys. Lett.* **100B**, 481 (1981).
[47] U. Heller, F. Karsch, *Nucl. Phys.* **B251**, 254 (1985).
[48] A. Di Giacomo, G. Paffuti, *Nucl. Phys.* **B205**, 313 (1982).
[49] J. Jurkiewicz, *Acta Phys. Pol.* **B18**, 311 (1987).
[50] H. Kawai, R. Nakayama, K. Seo, *Nucl. Phys.* **B189**, 40 (1981).